SPONTANEOUS IMBIBITION AND WETTABILITY CHARACTERISTICS OF POWDER RIVER BASIN COAL

A THESIS SUBMITTED TO THE DEPARTMENT OF PETROLEUM ENGINEERING

OF STANFORD UNIVERSITY

IN PARTIAL FULFILLMENT OF THE REQUIREMENTS FOR THE DEGREE OF MASTER OF SCIENCE

By
Tanmay Chaturvedi
June 2006

I certify that I have read this report and that in my opinion it is fully adequate, in scope and in quality, as partial fulfillment of the degree of Master of Science in Petroleum Engineering.

_____

Prof. Anthony R. Kovscek
(Principal Advisor)

I certify that I have read this report and that in my opinion it is fully adequate, in scope and in quality, as partial fulfillment of the degree of Master of Science in Petroleum Engineering.

_____

Dr. Louis Castanier

(Reader)

Abstract

We study the wettability of coal at scales that range from the microscopic to core to reservoir. While contact angle measurements define wettability at microscopic (pore) and core scales, relative permeability curves are used to define wettability and multiphase flow properties at core and reservoir scales. The microscopic wettability is evaluated based on the DLVO (Derjaguin, Landau, Verwey, Overbeek) theory. Estimates for contact angles have been made with variation in pH. The calculations suggest a trend in contact angle values with pH. The values go through a maximum at a pH around 4. They become small at low and high pH suggesting an alteration of coal wettability with pH and therefore with CO_2 dissolution in the systems. Water imbibition studies indicate that the core-scale wetness has similar trends as those obtained on the pore scale. Contact angle goes through a maximum at a pH of around 7 and is low in highly acidic and basic solutions. CT scanning based imbibition studies also provide a method of understanding multiphase flow in coal systems. Estimates for relative permeability of air-water flow in coal are obtained and reported. The results are encouraging as these are the first steps towards developing relative permeability curves for coal-methane and carbon-dioxide systems. These systems are important with regards to CO_2 sequestration and as well as enhanced methane production.

Acknowledgments

I would like to acknowledge the constant support and guidance provided by my advisor, Professor Anthony Kovscek. I would like to thank him for being available at all times to answer my queries and also for being extremely patient with my work.

I also greatly appreciate the help provided by Dr. Louis Castanier in keeping the CT scanner operable. With out his help any experiments with CT scanner would not have been possible.

I would also like to thank Dr. G. Tang for his help in the laboratory. All experiments that I performed would not have been possible without his help. His technical advice and guidance in the laboratory greatly reduced the time and effort that I had to put in and made experiments easier.

I would like to express my gratitude for the technical help provided by Dr. Josephina Schembre throughout my stay at Stanford. Working full time with Chevron she still found time to come to Stanford University to help me with my research.

This research was performed by funds provided by the 'Global Climate and Energy Project' at Stanford. The financial support provided is greatly acknowledged.

I would also like to express my gratitude to the SUPRI-A team for the valuable advice provided and for making research a lot of fun.

Finally I would like to thank my peers in the department who made my stay at Stanford extremely enjoyable. I will always have fond memories of the time I spent here.

Contents

Abstract v

Acknowledgments vii

Contents ix

List of Tables xi

List of Figures xiii

1. Introduction 1

1.1. Carbon Sequestration 1
1.2. Enhanced Coal Bed Methane (CBM) Recovery 2
1.3. Wettability of Coalbeds and Multiphase Flow 3
2. Interfacial Phenomena Using DLVO Theory 7

2.1. Modeling a CO_2 Coal Surface 7
2.2. Model Results 10
2.3. Wettability Sensitivity to Hamaker Constant 13
3. Experimental Setup and Data Processing 17

3.1. Manufacturing the Core 17
3.1.1. Manufacturing Process I 18
3.1.2. Manufacturing Process II - Core Press 19
3.2. Core Holder 22
3.3. CT scanning technique and applications 24
3.3.1. Scanning Artifacts and Beam Hardening 25
3.3.2. CT Scan Apparatus 25
3.4. pH Solution Preparation 27
3.5. Setting up the Apparatus 27
3.6. Saturation Initialization 28
3.7. Processing Image Data 29
3.8. FP Image Viewer 30
3.9. Relative Permeability from One Dimensional Saturation Profiles 31
3.10. ECLIPSE Model 33
3.11. B-Spline Curves 33
3.12. Modeling of Non-Equilibrium Effects 35
4. Results and Discussion 37

4.1. Macroscopic Contact Angle 37
4.2. Relative Permeability Estimations 41
4.3. Conclusions 46
Nomenclature 49

References 52

A. FPI Scripts 55
B. Matlab Codes for 1-Dimensional Saturation Profile Generation 63
C. Sample ECLIPSE 100 File for Relative Permeability Usage 65
D. Matlab Code for DLVO Calculations 70

List of Tables

Table 2-1: Zeta Potentials of air-water surface with varying salinity, Karakker and Radke (2002). ……...11

Table 2-2: Zeta Potentials of coal-water surface with varying salinity, Valverede(2003).12

Table 4-1: Amott Indices at various pH…….40

List of Figures

Figure 2-1: Variation in disjoining pressure with salinity…….12

Figure 2-2: Impact of Hamaker Constant on Wettability……..13

Figure 2-3: Summary of example calculations for contact angle on a coal surface. For reference, literature trends (Kelebek, 1982) are also indicated.....14

Figure2-4: Contact angle calculations for non-linear variation of Hamaker constant. The inset picture shows the two variations between $A=2*10^{20}$ J at pH 2 and $1*10^{20}$ J at pH 12.....15

Figure 2-5: Summary of example calculations for contact angle on a coal surface for constant charge. For reference, literature trends (Kelebek, 1982) are also indicated.....16

Figure 3-1: Non uniform imbibition…….18

Figure 3-2: Image shows a non uniform front during imbibition in a core made by manufacturing process one.....19

Figure 3-3: The various parts of the coal press……20

Figure 3-4: The various parts of the coal press……20

Figure 3-5: Preparation of the core using the coal press……..21

Figure 3-6: The core holder, coal pack, and endcaps……...22

Figure 3-7: The core holder with the core fixed inside it…….22

Figure 3-8: Schematic of the experimental apparatus……...23

Figure 3-9: Core Holder Inside the water jacket……...25

Figure 3-10: The water jacket used for imbibition studies……...26

Figure 3-11: Imbibition cell on the positioning system…….…..26

Figure 3-12: The Vacuum oven used for drying……...27

Figure 3-13: Apparatus to moisturize the core…….28

Figure 3-14: The complete experimental process using CT scanning……..29

Figure 3-15: The figures show a typical one-dimensional flow. Note the Sw scale on the right 30

Figure 3-16: Flowchart explaining the method used in relative permeability estimation. 33

Figure 4-1: Mass imbibition at different pH with cores made from first method…….38

Figure 4-2: Mass imbibition at different pH with cores made from second method…38

Figure 4-3: Mass imbibition at different pH with cores made from second method…39

Figure 4-4: Macroscopic wettability with pH variation……40

Figure 4-5: Saturation profiles with time for pH-2, flow is from right to left……...41

Figure 4-6: Simulation and experimental saturation profiles with time for pH-2…….42

Figure 4-7: Relative permeability curves, pH equals 2, air/water/coal system…….43

Figure 4-8: Simulation and experimental Saturation profiles for pH 10……..44

Figure 4-9: Relative permeability curves, pH equals 2, air/water/coal system…….44

Figure 4-10: Experimental and Simulation Saturation Profiles for pH equal to 7……45

Figure 4-11: Relative permeability curves, pH equals 7, air/water/coal system……...46

Chapter 1

1. Introduction

In this age of growing energy demand, there is an ever increasing need to find alternate sources of energy. There is also an urgent need to reduce the United States international dependence for energy. Along with the increase in the demand and consumption of energy the concentrations of carbon dioxide and other greenhouse gases in the atmosphere are also been found to be increasing (Keeling et. al., 1995). The amounts of these gases have more than tripled over the last century. The main reason for the steep increase is attributed to carbon emissions from fossil fuel burning and other human activities.

Several strategies including reduction in carbon emissions, reducing our dependence on fossil fuels, and improved efficiency are available to stabilize and moderate the emission of green house gases in the atmosphere. While the reduction of our dependence on fossil fuels is a long term measure as this would involve the transition to renewable energy resources such as wind, solar, and hydrogen fuel cell energy. A more current approach is **carbon sequestration.**

1.1. Carbon Sequestration

While the subject of greenhouse gas storage has been of great interest recently, the technology for this process is still in its incipient stages. Several technologies and processes are under consideration. Of these geologic sequestration holds specific importance. Here, the technique focuses on processes that sequester CO_2 in three types of subsurface formations: (1) saline aquifers, (2) oil and gas formations and (3) deep unmineable coal beds. The physical mechanisms of sequestration include, among others, dissolving the gas in reservoir fluids (brine solutions etc), trapping CO_2 as a gas or a super

critical fluid in geologic traps, and chemically reacting CO_2 with reservoir rock to produce mineral carbonates. We now look at a process that involves sequestering CO_2 in coal formations and also has the added advantage of producing natural gas.

1.2. Enhanced Coal Bed Methane (CBM) Recovery

Coal bed methane is a form of natural gas trapped inside coal seams and held in place by hydrostatic pressure. Although the major constituent of CBM is methane, the name is a misnomer as there are also other components associated with coal bed natural gas. Typically 88-98 % of this natural gas is methane. The rest is a mixture of higher alkanes and inorganic gases such as carbon dioxide and nitrogen (Diamond, 1986). Coal has large internal surface area that is of the order of 1 million square feet per pound of coal. This allows coal-beds to store 3-7 times the amount of methane per volume of rock as compared to that stored in conventional reservoirs. Not all coal beds on drilling show gas production, however, as most CBM occurrences are in coal seams submerged in an aquifer. CBM is stored primarily by physical adsorption as a mono-layer of gas on the coal surface. CBM is recovered when it desorbs from the surface as pressure in the reservoir declines.

The adsorption properties of coal are fundamental to gas injection and production. Two important pieces of information are obtained from an adsorption isotherm:

1. **The greater the pressure of the reservoir, the greater the amount of methane stored in the reservoir**. This implies that a deeper coal bed has a larger methane resource than a shallower one, for identical reservoir temperature. Also this explains the current technique of CBM recovery. Reservoirs are fractured to remove the water present thereby reducing the pressure. The amount of gas that remains adsorbed is reduced. The free gas is then collected by forcing the free gas to flow to producing wells.

2. **Different gases adsorb by different amounts on the same coal surface.** For example CO_2 adsorbs twice as much as methane. A more adsorbing gas displaces

a lesser adsorbing one at the same pressure. This explains the technique of enhanced CBM recovery where CO_2 is used to displace methane. The free gas is then captured in producing wells.

Carbon dioxide-enhanced coal bed methane (CO_2-ECBM), serves as one of the promising options for CO_2 sequestration. While the US has the largest deposits of coal in the world, 90% of these deposits are considered unmineable in terms of direct usage as a fossil fuel (US Coal Reserves, Review-1996). However, coal seams represent an attractive opportunity for near-term sequestration of large volumes of anthropogenic CO_2 at low net costs. For example, total CO_2 sequestration potential in coal beds within the US is estimated to be about 90 gigatons (Gt) (Reeves, 2003). For perspective, CO_2 emissions from power generation total about 2.2 Gt per year. Of this, 28-33% of it can be sequestered at a profit, and 89-95% of it can be sequestered at a cost of under $5 per ton, without considering CO_2 supply and transportation costs (Reeves, 2004). In most cases coal seams also provide a rich source of natural gas. In terms of methane recovery, the associated ECBM recovery potential is estimated to be over 150 trillion cubic feet (Tcf). By comparison; total CBM recoverable resources are estimated to be about 170 Tcf (Reeves, 2003). CO_2-ECBM has therefore the potential to sequester large volumes of CO_2 while improving the efficiency and potential profitability of natural gas recovery. Under all these factors, unmineable coal beds and the ECBM recovery technology appear to possess significant economic benefits.

1.3. Wettability of Coalbeds and Multiphase Flow

While multiple facets of CBM recovery using CO_2 are not well understood, our efforts are concentrated in understanding the change in wettability of coal surfaces during the ECBM process. Coal is a heterogeneous mixture of carboniferous plant remains and minerals (Drelich, 2001). These plant remains form coal macerals that are discrete organic entities in the coal with characteristic chemical and physical properties. One such property is wettability. A better understanding of coal wettability is important to comprehend how a coal surface behaves under the influence of various fluids such as methane, CO_2, and brine solutions. This behavior takes significance in understanding

multiphase flow and fluid redistributions in the coal matrix. Coal wettability is relatively well studied in the literature because of the importance of flotation to coal processing. Measurements of the contact angle, as measured through the water phase, range from 20 to 100 ° (e.g., Gutierrez-Rodrguez et al., 1984, Arnold and Aplan, 1989; Gowiewska et al.2002). The nonzero contact angle formed on coal surfaces varies with the pH of water and the coal source. On the other hand, some of the inorganic mineral matter in coal, so-called ash, is water wet. On a percentage basis by weight, ash may range typically from virtually zero to 20%. Thus, while a coalbed may be initially filled with water, the coalbed is largely formed of carbon in the form of coal that is not strongly water wet as evidenced by contact angles that are significantly nonzero.

Although the literature on coal flotation is not necessarily relevant to gas and water flow properties of coal, this data does indicate that careful consideration of the wettability of coal surfaces as a function of the salinity and pH of water is warranted. Additionally, there is relatively little understanding of the wettability of solid coal surfaces that have gases such as CO_2 and methane adsorbed to them. We have, therefore, directed our work towards understanding the multiphase flow properties of coalbeds containing carbon dioxide.

The water in a coalbed may vary from acidic to neutral to basic. Dissolved gases such as CO_2 reduce the pH of the water by forming carbonic acid. A typical CO_2-saturated water has a pH of 3.5. Given the substantial change in the pH of a coal water system due to the presence of dissolved CO_2, we have concentrated our efforts in determining the impact of pH on wettability of coal surfaces. Wettability of porous media, such as coal, is directly proportional to the ease with which the coal imbibes water spontaneously. We quantify wettability experimentally in terms of the rate of imbibition of water by coal. This quantification is also been used to determine multiphase flow properties of water and air in a variable pH coal-water system. Additionally, wettability is estimated from first principles in terms of the contact angle that is calculated for various pH using the Derjaguin-Frumkin equation (Hirasaki, 1990). Computation of relatively small contact angles suggests that the liquid spreads more readily and that imbibition rate is relatively

large, and vice versa. The primary input to the Derjaguin-Frumkin equation is the so-called disjoining pressure isotherm. It is a manifestation of surface forces that allow thin films to coat solids. The disjoining pressure characteristics of many practical systems are calculable from DLVO (Derjaguin, Landau, Verwey, Overbeek) theory (Israelachvili, 1991).

Chapter 2

2. Interfacial Phenomena Using DLVO Theory

2.1. Modeling a CO_2 Coal Surface

As discussed above, we are most interested in CBM systems in the presence of CO_2. To begin, we have assumed that the gas is at pressures less than the critical pressure. It follows that the major impact of CO_2 at these pressures is reduction in the pH of the solution. This is explained by the formation of carbonic acid (H_2CO_3). First, the wettability of coal as a function of pH is estimated. In the literature (Kelebek et al., 1982), the contact angles measured on a coal surface go through a maximum at a pH of 4 as pH is varied from 1 to 12. Our calculations to follow seek to reproduce such dependencies.

DLVO theory suggests that the interaction forces between a solid surface and a gas-water interface are either attractive or repulsive. The disjoining forces have three components: (1) structural forces, (2) van der Waals forces, and (3) electrostatic interactions originating from the overlap of ion clouds at each interface. The sum of these forces (F_h, F_A, F_d) results in the disjoining pressure, Π, between the surfaces.

Structural forces explain repulsion as two molecules come near each other. When the thick film ruptures, it forms a thin layer on the coal surface. This thin layer has dimensions of a few water molecule diameters. As the layer cannot be thinner then the diameter of a water molecule, the structural forces are modeled so as to become substantially repulsive at 0.3 nm which is the diameter of a water molecule. Churaev and Derjaguin(1984) have also suggested an attractive component to the structural forces for hydrophobic surfaces. We have, however, stuck to the conventional purely repulsive picture of structural forces. The forces in general are modeled as exponentially decreasing with increasing thickness of the film, h. These are taken to be of the form:

$$F_h = A_s \exp\left(-\frac{h}{h_o}\right) \qquad \textbf{2-1}$$

Here A_s depends upon the type of system and h_o is the decay length. We have used values as suggested by Hirasaki (1990) who states that a typical value of h_o is 0.05 nm.

van der Waals forces are dependent on the distance between any two surfaces. For thin film interaction, van der waals forces are given as (Buckley *et al.*, 1989):

$$F_A = -\frac{A}{12\pi h^3}\frac{\left(15.96\frac{h}{\lambda}+2\right)}{\left(1+5.32\frac{h}{\lambda}\right)^2} \qquad \textbf{2-2}$$

Here h is the distance between the gas-water interface and the coal surface, 'A' is the Hamaker constant, and λ is the London wavelength that is approximately 100 nm for most systems. The Hamaker constant is either measured or calculated by Lifshitz theory, as explained in detail later.

The two surfaces of a colloidal thin film interact as a result of the presence of ionic charge on these surfaces. The forces between the two surfaces are usually calculated by modeling the surfaces as either constant potential or constant surface charge. Mathematical expressions were developed by Gregory (1981) for both cases as well as an intermediate case.

The constant potential case of Gregory (1981), is formulated as

$$F_d = n_b kT \frac{\left(2\varphi_1\varphi_2\cosh(\kappa h)+\varphi_1^2+\varphi_2^2\right)}{\left(\sinh(\kappa h)^2\right)} \qquad \textbf{2-3}$$

whereas the constant surface charge is formulated as

$$F_d = n_b kT \frac{\left(2\varphi_1\varphi_2\cosh(\kappa h)-\varphi_1^2-\varphi_2^2\right)}{\left(\sinh(\kappa h)^2\right)} \qquad \textbf{2-4}$$

Here, φ_1 and φ_2 are reduced potentials that are written as

$$\varphi_1 = \frac{e\zeta_1}{kT} \qquad \textbf{2-5}$$

$$\varphi_2 = \frac{e\zeta_2}{kT} \qquad \textbf{2-6}$$

In Eqs, (2-3) to (2-6), the symbols κ is the inverse Debye length ($\kappa = \left(\frac{2n_b e^2}{\varepsilon kT}\right)^{.5}$), ζ is the surface potential that is commonly taken as the zeta potential, k is Boltzmann's constant ($1.38*10^{-23}$ J/K), n_b is the ion density, e is the electronic charge ($1.6*10^{-19}$ C), ε is the electric permittivity ($7.08x10^{-10}$ C^2/N-m^2), and T is absolute temperature. Temperature is assumed constant at 300K.

According to Gregory (1981) most cases lie somewhere in between the constant potential and the constant charge case. He proposed a linear superposition of the two cases giving:

$$F_d = 64 n_b kT \varphi_1 \varphi_2 \exp(-\kappa h) \qquad \textbf{2-7}$$

were

$$\varphi_1 = \tanh\left(\frac{\zeta_1}{4}\right) \qquad \textbf{2-8}$$

$$\varphi_2 = \tanh\left(\frac{\zeta_2}{4}\right) \qquad \textbf{2-9}$$

Calculation of the wettability of a surface is accomplished, by first summing the individual contributions of thin-film forces to the disjoining pressure:

$$\Pi(h) = F_h(h) + F_A(h) + F_d(h) \qquad \textbf{2-10}$$

Direct integration of the augmented Young-Laplace equation of capillarity yields

$$P_c = \sigma C_m + \Pi(h) \qquad \textbf{2-11}$$

Here C_m is the interfacial curvature. The relationship between equilibrium contact angle , θ, and disjoining pressure (Derjaguin, 1940) follows

$$\cos\theta = 1 + \frac{1}{\sigma}\left(\int_h^\infty \pi(h)dh + h\pi(h)\right) \qquad \textbf{2-12}$$

Again, h is the equilibrium film thickness of interest.

2.2. Model Results

A numerical code was developed to calculate the disjoining pressure curve and the contact angles for the variety of conditions expected. The input parameters are the number of ions formed, molar concentration and the zeta potential values at the two surfaces. Using DLVO theory and the definitions of different forces, we calculate the disjoining pressure curve, Eq. (2-10). This is then used to calculate the contact angle, Eq. (2-12). The algorithm is summarized as follows.

- Assume constant potential or constant charge.
- Calculate π for h ranging from 0.01nm to 100nm.
- Calculate θ based on a limiting thickness of thin film; hence, if the limiting thickness is h=a, the area under the disjoining pressure curve is calculated from h=a to h=100nm.
- Finally, add $\pi(a)a$ to the integral and to calculate θ.

For generality, calculations were made for a number of thicknesses assuming the film to be 1 to 4 layers of water molecules. There are a variety of inputs needed to conduct calculations of wettability using Eq. (2-12). These include zeta potential at different pH, the Hamaker constant and structural force parameters. The zeta potential data for the vapor-water surface is taken from Karakker and Radke (2002). They developed a model for the interface based on the Gibb's adsorption isotherm. This model compares well with data collected by Li and Somasundaram(1991). For the coal water surface we used the ionizable surface group model developed by Valverede *et.al*. (2003).

Uncertainty exists regarding values of the Hamaker constant and structural forces relevant to the coal-water system. We have modeled these physical quantities for the coal-water-CO_2 system based on limited data available in the literature. Table 2-1, 2-2 represent the literature data used for calculations. A sensitivity analysis is summarized to determine and predict the parameters that most influence wettability and to what extent. The salinity decides the molar ion density and therefore the strength of the electrostatic forces as

compared to the other components. For the case of coal and acidic water, it was seen that the forces become more attractive with increasing salinity. Example dependencies are shown in Figure.2-1. The contact angle decreases with increasing salinity, according to Eq. (12). Figure 1 illustrates an important aspect of coal surfaces. Consider a film on an uncurved surface where C_m is equal to 0. Equation (2-11) then indicates that P_c is equal to Π. For positive nonzero capillary pressures, all equilibrium films, corresponding to the curve in Fig. 2-1, are quite thin and of order 0.4 nm. Thus, water does not form thick wetting films on such surfaces and contact angles are strictly non zero for such Π versus h relationships.

Table 2-1: Zeta Potentials of air-water surface with varying salinity, Karakker and Radke (2002).

Salinity 0.01		Data Points		Model		Our best fit curve
	pH	Zeta	pH	zeta	pH	zeta
	2	-0.01	2	-0.005	2	-0.01946
	2.7	-0.025	4	-0.017	3	-0.03084
	3.2	-0.023	6	-0.018	4	-0.03892
	3.9	-0.033	8	-0.018	5	-0.04518
	4.5	-0.034	10	-0.018	6	-0.0503
	5.8	-0.039	12	-0.018	7	-0.05463
	8.2	-0.06			8	-.05858
	9	-0.05			9	-.06168
	10	-0.065			10	-.06464
	11	-0.075			11	-.06732
	11.8	-0.06			12	-.06976
Salinity 0.1	2	-0.008	2	-0.004	2	-0.001
	2.8	-0.017	4	-0.005	4	-0.006
	4	-0.013	6	-0.006	6	-0.008
	4.5	-0.02	8	-0.006	8	-0.010
	5.5	-0.02	10	-0.006	10	-0.012
	7.8	-0.02	12	-0.006		
	10	-0.04				

Table 2-2: Zeta Potentials of coal-water surface with varying salinity, Valverede(2003).

Salinity 0.01		Data Points		Model		Our best fit curve
	pH	zeta	pH	Zeta	pH	zeta
	3.3	0.005312	2	0.011	2	0.011389
	3.8	0.00399	4	0.0032	3	0.007902
	4.6	-0.005312	6	0.01966	4	0.003201
	5.8	-0.015	8	-0.025	5	-0.00531
	6.2	-0.0142	10	-0.028	6	-0.0142
	7	-0.028	12	-0.0296	7	-0.02059
	8.7	-0.024			8	-0.02507
	10.8	-0.0269			9	-0.02693
					10	-0.02821
					11	-0.02891
					12	-0.02959
	3.2	0.000	2	0.002	3	0.015
	3.3	-0.001	4	-0.013	4	0.011
	4.2	-0.018	6	-0.034	5	0.008
Salinity 0.1	4.5	-0.015	8	-0.040	6	0.005
	5.2	-0.031	10	-0.042	7	0.003
	6	-0.040	12	-0.042	8	0.001
	6.8	-0.040			9	0.000
	8.2	-0.037			10	-0.002
	11	-0.034			11	-0.003

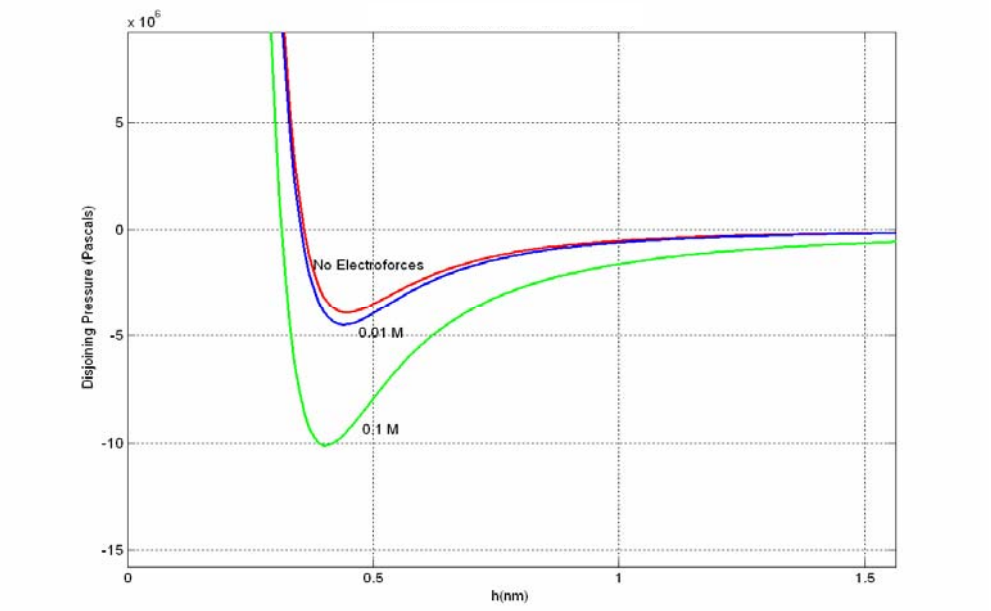

Figure 2-1: Variation in disjoining pressure with salinity.

2.3. Wettability Sensitivity to Hamaker Constant

Hamaker constants are computed in terms of the refractive index and the dielectric permittivity of the fluid (Israelachivili, 1991). The Hamaker constant based on this theory is found as the sum of two terms: the static dielectric term and a second term evaluated on the basis of using dielectric constants at imaginary frequencies. The equation is written as

$$A = \frac{3}{4kt}\left(\frac{(\varepsilon_1-\varepsilon_3)(\varepsilon_2-\varepsilon_3)}{((\varepsilon_1-\varepsilon_3)(\varepsilon_2-\varepsilon_3))}\right)+\frac{3}{8\sqrt{2}}\left(\frac{\left(n_1^2-n_3^2\right)\left(n_2^2-n_3^2\right)}{\left(\sqrt{\left(n_1^2+n_3^2\right)\left(n_2^2+n_3^2\right)}\right)\left(\left(\sqrt{n_1^2+n_3^2}\right)+\left(\sqrt{n_2^2+n_3^2}\right)\right)}\right) \quad \textbf{2-13}$$

Here ε are the dielectric constants and n are the refractive indices. The subscripts 1 and 3 represent the different phases, solid and vapor, and the subscript 2 represents the separating medium, water. Hamaker constant values are of the order of $1x10^{-20}$J, however, they vary from system to system. As little is known about the Hamaker constant of the coal surface, we performed a sensitivity analysis on the impact of Hamaker constants on wettability of coal surfaces. We varied the Hamaker constant from $1x10^{-20}$J to $1x10^{-19}$J. Figure 2-2 shows the impact of varying Hamaker on wettability with pH. The 3 different curves represent Hamaker values of 1,5 and 10($x10^{-20}$J).

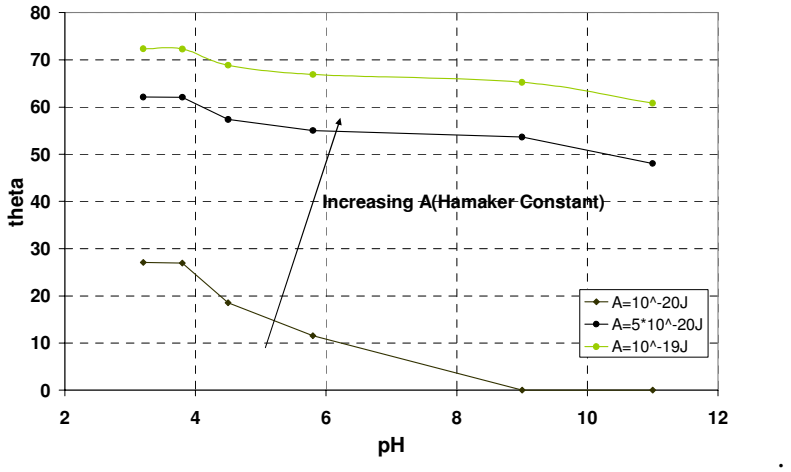

Figure 2-2: Impact of Hamaker Constant on Wettability.

An increase in the Hamaker constant results in greater contact angle values. This is because an increase in Hamaker constant is equivalent to increasing the contribution of

van der Waals forces in the disjoining pressure calculation. van der Waals forces in turn are attractive forces and increase the negative value of the area under the disjoining pressure curve. By Equation 2-12 we see that this results in smaller values of the cosine of the contact angle. Thus contact angle values are sensitive to the Hamaker constant. An order of magnitude increase in the Hamaker constant substantially alters the wettability of the system.

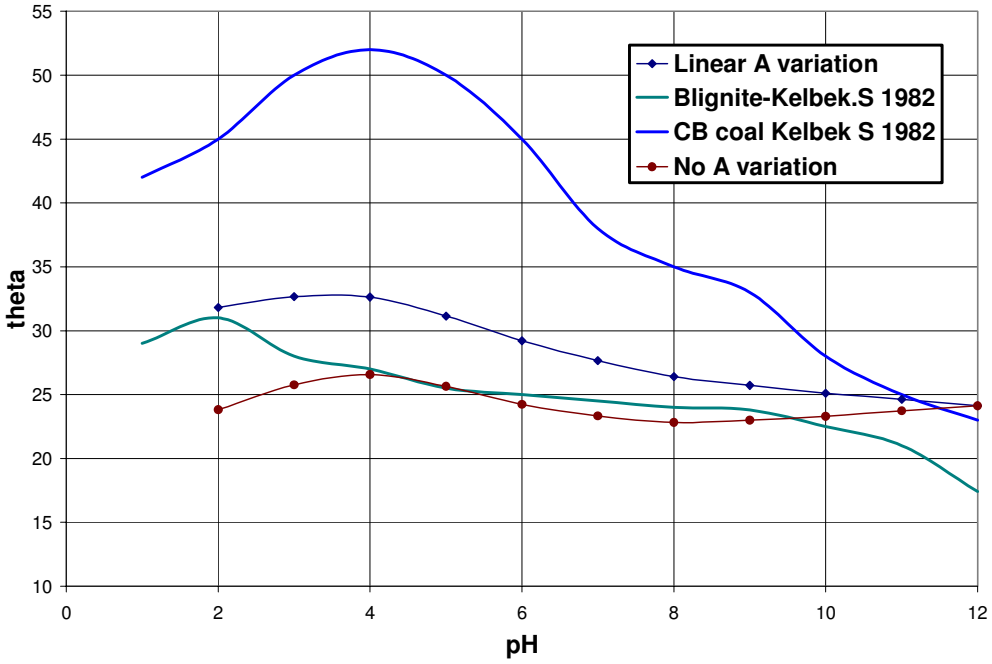

Figure 2-3: Summary of example calculations for contact angle on a coal surface. For reference, literature trends (Kelebek, 1982) are also indicated.

The analysis above provides us an important tool to model wettability alterations of coal-water systems with pH. In the literature Hamaker constants are generally assumed constant for a given system. For significant pH variation from 3 to 12, however, Eq. (2-13) indicates that the Hamaker constant varies because it depends on the dielectric properties of the medium, of the coal surface and the vapor. Amongst these, the dielectric properties of water experience the most significant change with variation of pH (Weast, 1983). Representative disjoining pressure and contact angle calculations were made assuming firstly a constant Hamaker constant 10^{-20} J. and secondly a linearly varying Hamaker constant. In the latter case, the linear variation of A is from $1x10^{-20}$J at a pH of 2 to $2x10^{-20}$ J at a pH of 12. Figure 2-3 summarizes results for a constant potential. For

reference, measured contact angle data for two different coals is also presented. A linear variation of A with pH yields contact angle functionality most similar to the experimental data presented in the literature. A maximum contact angle is found at a pH of 4 and coal becomes progressively more water wet as the wetting solution becomes more basic or acidic.

We also looked at non-linear variations of Hamaker constant. Figure 2-4 summarizes the results obtained for two sets of such variations. The first curve is a convex variation of the Hamaker constant. The values vary from $A=2*10^{20}J$ at pH 2 and $A=10^{20}J$ at pH 12. The calculations were based on the best fit curves for data points from literature (refer Tables 2-1, 2-2) at 0.01molar salinity. As suggested earlier, results show that contact angles are sensitive to Hamaker constant. However for any value of Hamaker constant high pH solutions seem to be much more water wet than neutral solutions. At low pH, these profiles also suggest a decrease in the contact angles. This follows the trends as suggested by literature and experimental calculations.

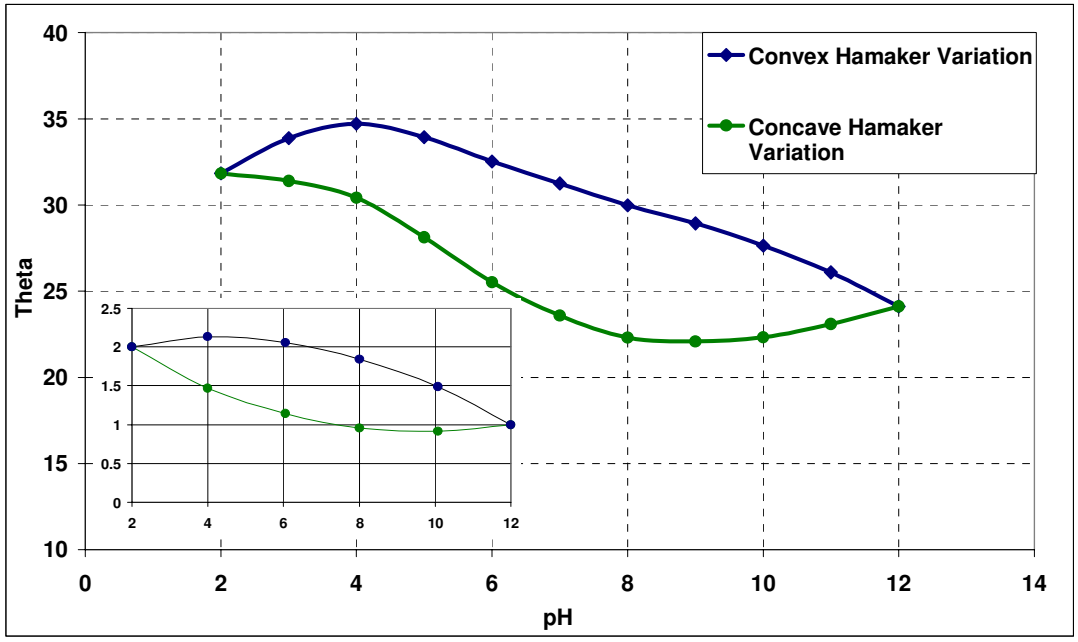

Figure2-4: Contact angle calculations for non-linear variation of Hamaker constant. The inset picture shows the two variations between $A=2*10^{20}$ J at pH 2 and $1*10^{20}$ J at pH 12.

Figure 2-5, summarizes results for constant charge. A constantly charged surface tends to be highly water wet in a basic environment. The sensitivity to pH is also much greater for a constantly charged surface. Figure 2-3 and 2-5 suggest that while it is not easy to assess the nature of the coal and thin film surfaces, thin films in coal systems have a tendency to be at constant potential.

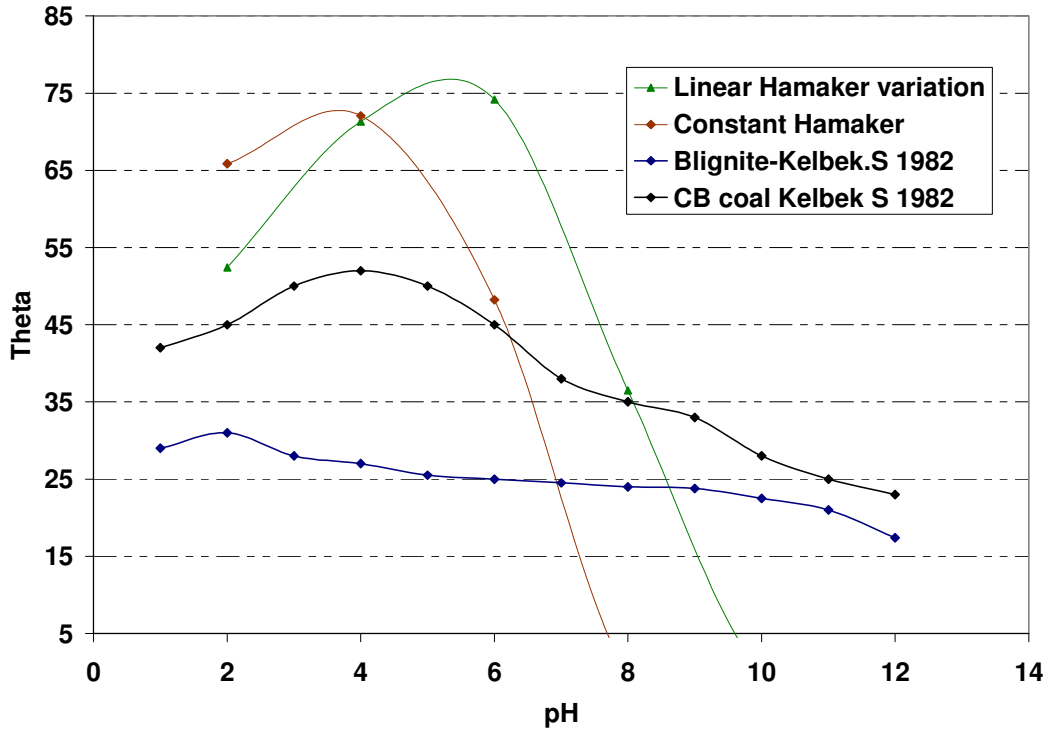

Figure 2-5: Summary of example calculations for contact angle on a coal surface for constant charge. For reference, literature trends (Kelebek, 1982) are also indicated.

The disjoining pressure calculations presented in Figure 2-1 teach that thin water films on coal surfaces are quite thin, possibly on the order of one or several layers of water molecules. In this case, short-range structural forces within thin films become important. As stated earlier, the values of A_s and h_o are system dependent. For the coal, water, and CO_2 system these values have not been studied. The magnitude of A_s was varied over 3 orders of magnitude to check impact on contact angle calculations. Sensitivity of the computed contact values is small and the contact angle is always nonzero.

Chapter 3

3. Experimental Setup and Data Processing

The modeling and literature review above suggests that the contact angle of coal surfaces varies with the chemistry of the wetting solution. In terms of spontaneous imbibition of water into coal, the imbibition rate should be a function of solution pH. As the contact angle changes, so does the rate of imbibition. Our experimental effort was aimed at verifying the above predictions.

3.1. Manufacturing the Core

Coal in general is extremely brittle. Most coal cores break up into chunks even before they can be processed for the purpose of experiments. We therefore have manufactured our own core using coal powder from the Powder River basin in Wyoming. The coal samples were obtained from a formation depth of about 900-1200 ft. The coal was ground to a size of 60 mesh (mean size 0.25 mm). The coal powder was pressed to develop cores for imbibition studies. We applied two methods to make the cores, as described shortly. Cores were found to have a greater permeability and porosity values than actual coal matrix. While the high porosity and permeability of coal cores produced, as such, suggests that these cores are incapable of reproducing the actual flow conditions, the utility of such coal cores lies in understanding the relative flow of gas and water and understanding the affinity of these fluids for coal surfaces. Multiphase flow is a strong function of the chemical composition of the system as compared to absolute physical quantities such as porosity, permeability etc. The chemical composition is macroscopically quantified in terms of wettability. It is this property of the system that we endeavor to study and therefore the usage of our *'homemade'* cores is justified.

3.1.1. Manufacturing Process I

The first method involved hammering the coal into an acrylic cylinder. This was done with help of wooden dowel and a hammer. The powdered coal was compressed and forced into an acrylic core holder. Each end of the core holder is capped with stainless steel mesh screen of a size small enough to retain coal particles. Two cores were constructed identically to allow dual experiments to be conducted. While the cores developed by this method gave us interesting results, there were certain problems during dynamic experiments.

These cores were found to be quite heterogenous. Figure 3-1 shows the water saturation profile of the core with time. There can be seen random bumps in the curve suggesting changes in porosity and permeability along the length of the core. This was because of the non-uniformity of the force applied when the coal was packed. Figure 3-2 is an image of imbibition in a core made by the first process. Note the darkly shaded water. The image illustrates the problems faced in attaining a one-dimensional flow profile using cores made by the first process. Finally, it is interesting to note that Fig. 3-1 displays clear differences in slope despite all of the problems listed above.

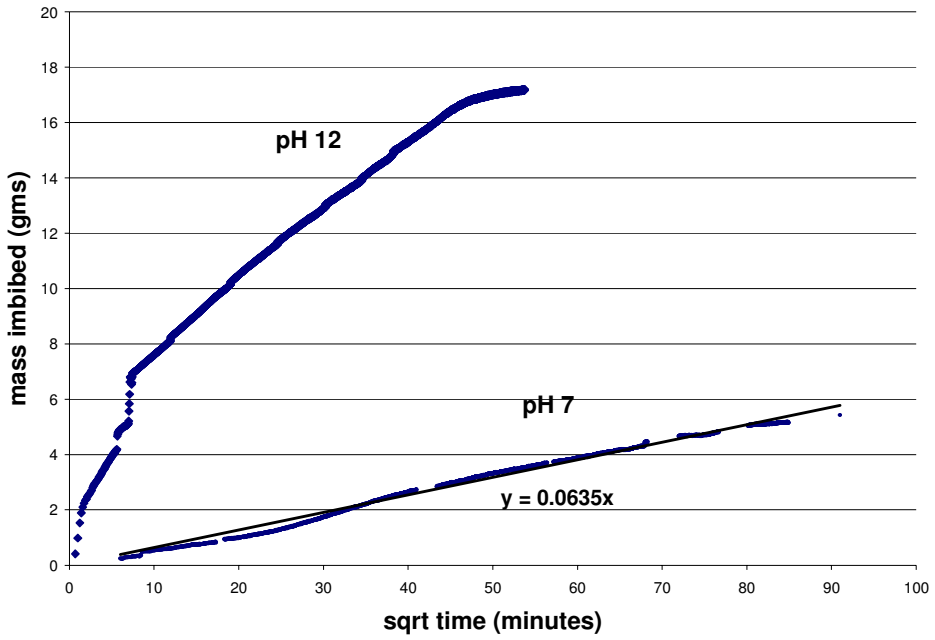

Figure 3-1: Non uniform imbibition.

The inability to produce uniform one dimensional flow in cores manufactured by the first method made us shift to the second method that uses a press. The press allowed us to produce much more uniform cores. Also, the porosity and permeability achieved with a uniform press is smaller than those obtained by manually packing the coal. They are also much closer to actual coal systems.

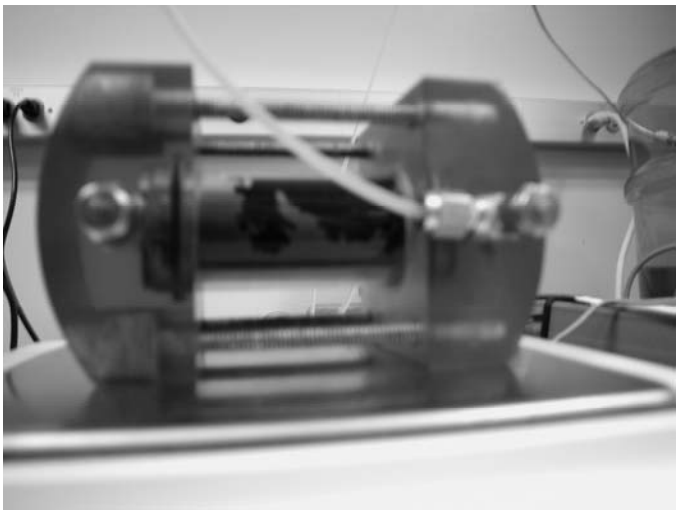

Figure 3-2: Image shows a non uniform front during imbibition in a core made by manufacturing process one.

3.1.2. Manufacturing Process II - Core Press

The second method involved a press to manufacture more homogeneous cores. This was done using a press designed in our labs. Figure 3-3 & 3-4 illustrate the press and explains its various parts.

The press consists of the following main parts:

- main annulus where the coal for the core is placed,
- a screw cap on one end ,
- a screw with a flat head to press the coal in , and
- a key to rotate the screw .

The main annulus consists of two hemi-cylindrical parts that are screwed together. The annulus is lined with an aluminum foil. This prevents coal particles from adhering to the sides of the annulus. The aluminum foil also provides support to the packed core when it

is taken out. Turning the key rotates the flat headed screw that is used to pack the coal in the annulus. The cap at the bottom provides support as the screw packs the coal.

Figure 3-3: The various parts of the coal press.

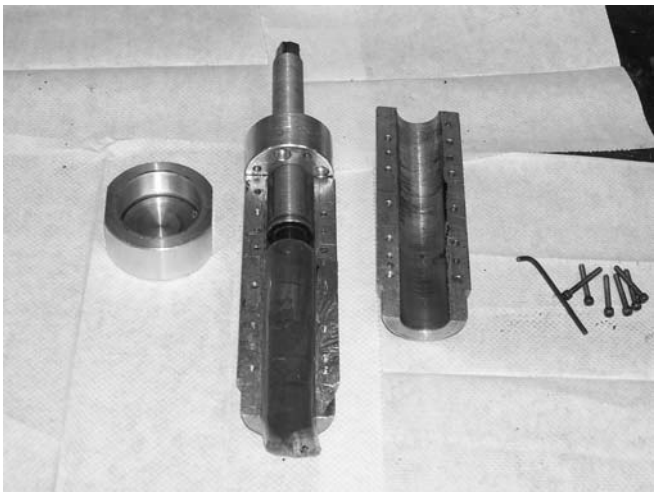

Figure 3-4: The various parts of the coal press.

Figure 3-5 illustrates the process of coal packing. With coal inside the annulus the screw is rotated using the two handled key. A small amount of water is added as the screw rotates down. This allows the coal powder to coalesce together, reducing the volume occupied. The procedure of packing the coal requires twisting the screw every few hours for a day as it takes some time for the pressure to be transferred to the bottom of the core.

Once the coal has been packed, the end cap is unscrewed and a steel cylinder is used to push out the core from the press. The core is then set with epoxy in an acrylic cylinder. The diameter of the cylinder is much larger than the core. The space between the core and the walls of the cylinder is filled with epoxy. This is done to ensure that the core sticks to the walls of the cylinder and to prevent channeling of any fluids along the core surface. Once the epoxy sets, the cylinder is machined to the size of the core holder using a lathe. The core is then set in the core holder as shown in Figure 3-6.

Figure 3-5: Preparation of the core using the coal press.

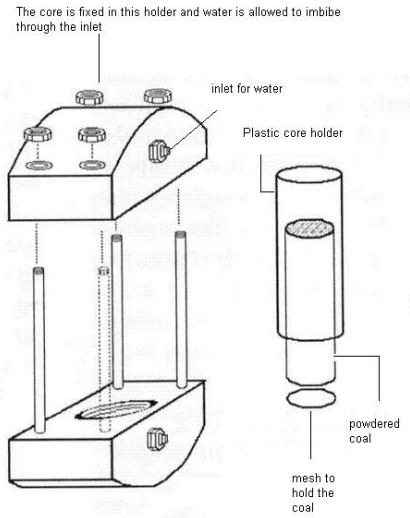

Figure 3-6: The core holder, coal pack, and endcaps.

3.2. Core Holder

The core holder consists of two end caps that hold the core in place. The endcaps of the core holder were constructed to allow for both counter and co-current imbibition. During a countercurrent experiment, water flows through the endcap and across the face of the coalpack. The endcap contains a 5 mm gap through which water flows and provides a supply of fresh water at the face of the coalpack. Each end of the core holder is capped with stainless steel mesh of a size small enough to retain coal particles. Figure 3-7 illustrates the core holder with the core fixed in the interior.

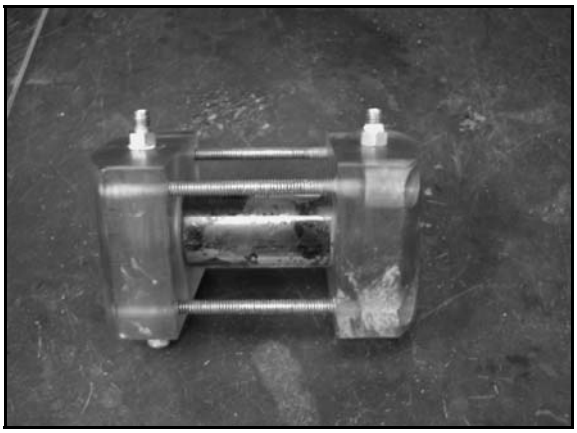

Figure 3-7: The core holder with the core fixed inside it.

Initial experiments were done with a simple apparatus. Figure 3-8 illustrates the experimental set up. The cores made by hammering in the coal are dried under vacuum for at least 48 hours until core weight became constant. The core is then fixed in the core holder and the core holder is then set on an electronic balance. The tubings from a beaker of given pH solution are connected to one of the outlets to the core and also to the suction pump. The suction pump draws the pH solution from the beaker and supplies it to the core as seen in the figure. The valves are set so that flow through the coalpack is countercurrent, the balance was zeroed, data collection begins, and the pump circulates water through the endcap and across the face of the coal pack at a rate of 1 cm^3/min.

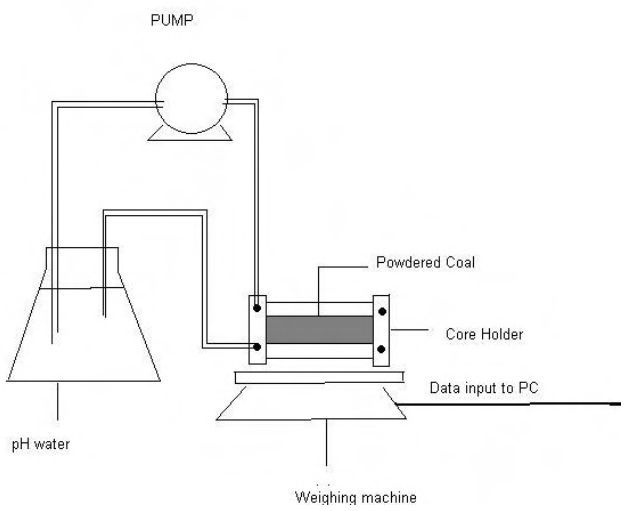

Figure 3-8: Schematic of the experimental apparatus.

Classical water imbibition theory is used to interpret the data collected. Handy (1960) derived an approximate equation relating the mass of water imbibed, m, with capillarity and wettability that reads

$$m = \rho_w A\sqrt{2P_c k\varphi S_w t/\mu} \qquad 3\text{-}1$$

where ρ_w is the density of water, A is the cross sectional area, P_c is the capillary pressure, k is the permeability, ϕ is the porosity, S_w is the saturation, μ_w is the viscosity of water and t is the time. The slope of the lines, with respect to $t^{1/2}$, is then equal to $\rho_w A\sqrt{2P_c k\varphi S_w/\mu}$. Next, the capillary pressure, Eq. (3-2) is substituted into Eq. (3-1)

$$P_c = \sigma \cos\theta \sqrt{\frac{\varphi}{k}} J(S_w) \qquad 3\text{-}2$$

Among different pH solutions, P_c differs by a factor of $\cos\theta$ because $J(S_w)$ is unique for similar coalpacks and the interfacial tension, σ, is sensibly independent of pH. So from imbibition data collected at two different pH's, we obtain the following ratio of mass imbibed

$$\frac{m_1}{m_2} = \left(\sqrt{\frac{\cos\theta_1 S_{w1}}{\cos\theta_2 S_{w2}}} \right) \qquad \textbf{3-3}$$

All quantities, except the ratio $\cos\theta_1/\cos\theta_2$ are measured. These measurements then indicate the relative change of contact angle with pH.

3.3. CT scanning technique and applications

While the results from these initial experiments are interesting, not much information about real time saturation distributions inside the core is obtained. We therefore also performed our experiments using the technique of CT scanning.

Computed tomography allows non-destructive evaluation of flow in porous media. Its advantage lies in the fact that you obtain real-time images of the media and information about real time saturation distributions in the core. The technique involves the study of the core under a beam of X-rays. The rays are rotated around the core in single planes and cross-sectional images of the core are developed using information obtained from the attenuation of the X-rays. Different materials attenuate X-rays to different extents. Therefore, based on the intensity of the transmitted rays, we measure the fluid distribution in the core. The CT scanner is first calibrated by attributing a CT number to the fluids of interest. In our case, these are water and air, with CT number values 0 and -1000, respectively. Then based on the intensity of the transmitted X-rays, the CT scanner evaluates a voxel by voxel CT number. These numbers are then used to estimate porosity and saturation values at each voxel of the core.

The equations involved in determining the porosity and saturation values from CT numbers are the following (Akin and Kovscek, 1998):

$$\phi = \frac{CT_{wet} - CT_{dry}}{CT_{water} - CT_{air}} \qquad \textbf{3-4}$$

$$S_w = \frac{CT_{obj} - CT_{dry}}{CT_{wet} - CT_{dry}} \qquad \textbf{3-5}$$

3.3.1. Scanning Artifacts and Beam Hardening

X-ray CT scanning is subject to errors and image artifacts resulting from apparatus design and materials. Most of these artifacts are explained in terms of 'beam hardening'. Beam hardening refers to the shift of the attenuated X-ray beams to higher energy. This is due to preferential absorption of a portion of the beam spectra by the media. Beam hardening is manifested as dark bands around the periphery of the object. These artifacts are minimized by using an apparatus design that removes these effects from the portion of the image that is of interest. We therefore place our core holder inside a water jacket.

3.3.2. CT Scan Apparatus

Figures 3-9 and 3-10 illustrate the use of the water jacket. The water jacket consists of a cylindrical vessel closed at both ends by circular plastic end plates.

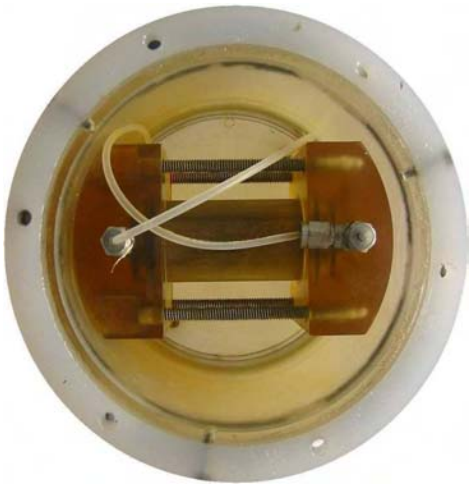

Figure 3-9: Core Holder Inside the water jacket.

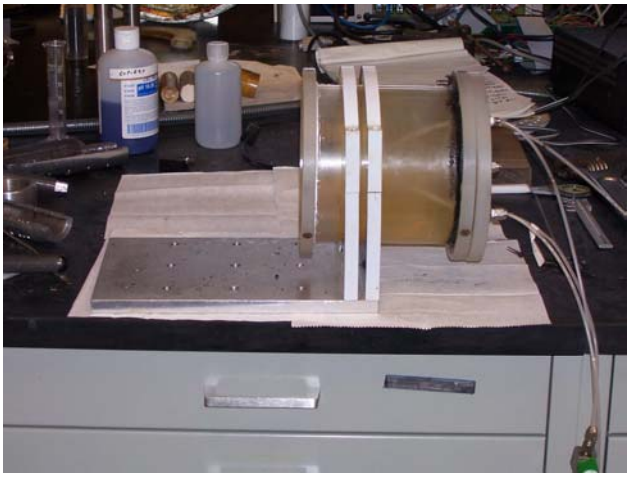

Figure 3-10: The water jacket used for imbibition studies.

The core is placed horizontally inside the water jacket. The tubing leading through the connections at the in/out lets of the core holder come out through holes in the circular end plates. Once the core holder is set inside the water jacket, the jacket is filled up with water through a valve in the center of one of the disks. The cylindrical vessel is attached to an aluminum mounting plate that is screwed on to the positioning system of the CT scanner. Figure 3-11 illustrates the imbibition cell on the positioning system.

Figure 3-11: Imbibition cell on the positioning system.

3.4. pH Solution Preparation

The experiments require water solutions of varying pH. We have used solutions of pH equal to 2, 3.6,5,7 and pH 10 for our experiments. The acidic solutions were prepared using distilled water and concentrated HCL solutions. The basic solutions were prepared by dissolving NaOH pellets in distilled water. A Fischer Scientific pH meter was used to measure pH values with an accuracy of 1%.

3.5. Setting up the Apparatus

The experiment begins with drying the core, until there is no weight change. This is done in a vacuum oven. Figure 3-12 shows the apparatus used for drying the core. The temperature of the oven is maintained at 35°C. The process of drying the core takes about 3-4 days. When the weight of the core no longer changes, the core is then ready for the experiment.

Figure 3-12: **The Vacuum oven used for drying.**

3.6. Saturation Initialization

The core is initially saturated to low water saturation. We have kept this saturation at about (8±2)%. This is done by forcing moist air through the core. Figure 3-13 shows the apparatus used for this purpose. One outlet of the core holder is connected to house vacuum. The opposite outlet is connected via tubing to a glass vessel half filled with water. The bottle has another piece of metal tubing. This tubing is opened to the atmosphere. On switching on the vacuum, air from the atmosphere is sucked into the bottle. This air travels through the water and is then transported as moist air into the core. The initial saturation is then evaluated based on the weight gained by the core.

The core is then placed along with the core holder in a water jacket. Once the core is set horizontally inside the water jacket, the water jacket is filled up with water and screwed onto the CT scanner positioning system. The water jacket on the moving table is set centrally in the X-ray chamber.

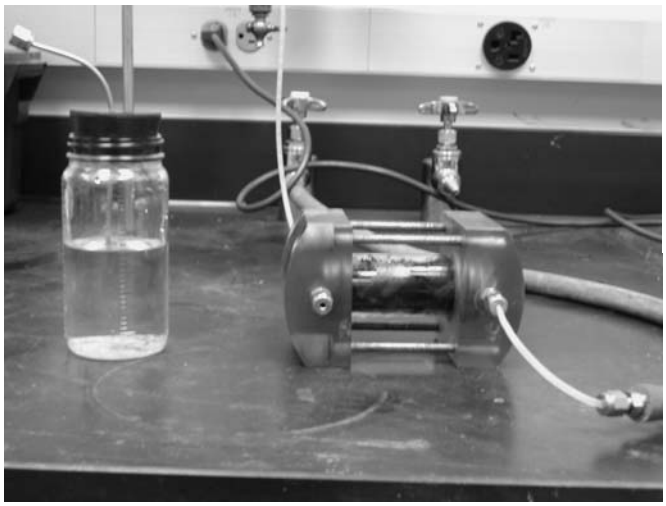

Figure 3-13: **Apparatus to moisturize the core**

The pH solutions prepared as suggested above are kept in a beaker whose top is covered with aluminum foil. This is done to avoid any evaporation of solution during the experiment. All leaks in the foil are made airtight by applying epoxy. The air tight beaker is then placed on an electronic balance. The weight loss is recorded by real time transfer of data to the computer. Figure 3-14 shows the complete procedure.

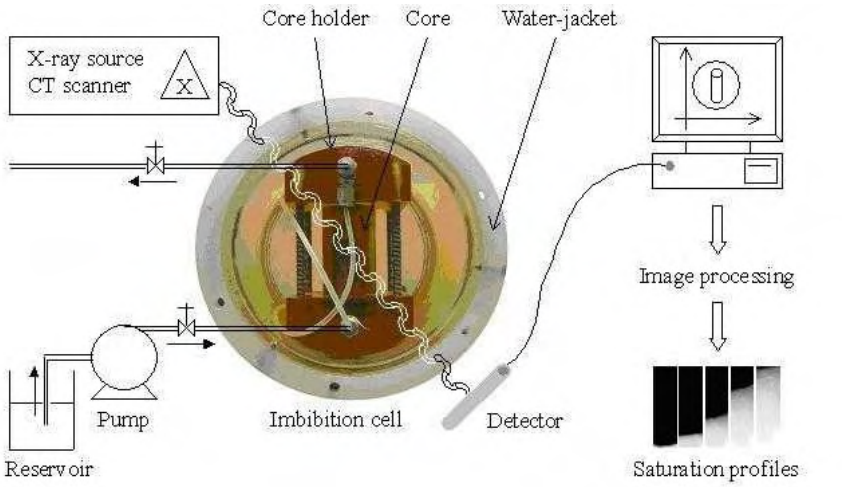

Figure 3-14: The complete experimental process using CT scanning.

The core is scanned every minute initially to capture end effects, and then every few minutes varying from 5 to 30 minutes depending on the solution and whether there is a fracture. The change in weight is captured every 30 seconds. At the end of spontaneous imbibition, a forced imbibition is conducted to saturate completely the core with water. This is required for evaluating real time saturation profiles and the Amott wettability index.

3.7. Processing Image Data

The flow in the core is one dimensional. That is, the capillary forces in the direction of the length of the core dominate over all other flow forces in the core. The length of the core is small enough that the gravitational forces are insignificant. Also as the core is homogeneous and the whole face of the core is charged with water, the flow in any radial direction becomes unimportant. One dimensional flow is also validated by the almost flat saturation fronts of the obtained CT images. Figure 3-15 shown below illustrates the 1-D nature of the flow.

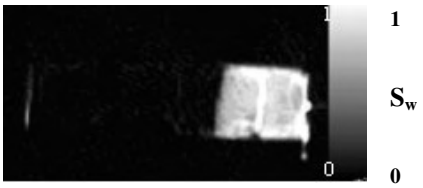

15 minutes

30 minutes

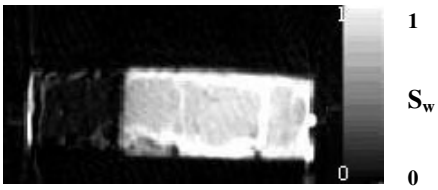

180 minutes

Fully saturated

Figure 3-15: The figures show a typical one-dimensional flow. Note the Sw scale on the right

3.8. FP Image Viewer

The data obtained from CT scanning are used to obtain 1 dimensional saturation profiles. The image data obtained from a CT scanner contains information about the core in terms of matrices of CT numbers. These matrices are manipulated using an FP image viewer. Images are first saved in a folder easily accessible by FP image viewer. They are then loaded into the viewer as a complete image set. An image set is processed by applying a script to these images, Appendix A. A script is a set of commands written using specific keywords that when applied to a set of images helps you perform some mathematical transformations on the images. Separate scripts were written to evaluate the voxel by voxel porosity of the core and to evaluate the voxel by voxel saturation in the core, Appendix A.

The images thus achieved gave us the saturation profiles in the core with time. To obtain a one dimensional profile from these images, we compute a weighted saturation value at each vertical cross section of the core. For this purpose we used MATLAB to process the images. Saturation profiles for all times were input into MATLAB. A small program was written that evaluated weighted saturations along the profile of the core, Appendix B.

These weighted saturations were then normalized based on a total mass balance. At each point in time we know the amount of water imbibed into the core. This provides the total saturation of the core. The area under the saturation curve equals the ratio of water imbibed to the water imbibed at complete saturation. Equation 3-6 mathematically explains the material balance. The length of the core was also normalized to 1.

$$\int_0^1 S(\xi)\, d\xi = \textbf{wt of water imbibed/ wt of water imbibed at complete saturation} \qquad \textbf{3-6}$$

This was done for values of pH equal to 2, 7 and 10. The one dimensional profiles are useful in evaluating the relative permeability curves of the system.

3.9. Relative Permeability from One Dimensional Saturation Profiles

While contact angles provide important information about coal surfaces in the presence of multiple fluids, a more important and relevant quantity in reservoir engineering is relative permeability. Understanding how fluids (methane/CO_2, water) flow in the reservoir helps us in developing solutions for current problems. For example, current CBM processes are associated with very large water production rates. Disposal of this produced water is a significant contributor to Field operation expenses. Implementing conditions that alter the relative permeability of water so as to reduce production rates therefore becomes an important area of study. In our study we have, therefore, attempted to develop relative permeability profiles for the modeled CO_2 – coal surface. We have used the method developed by Schembre & Kovscek (Schembre, 2004) for our calculations. The method is based on minimizing the error between experimentally measured saturation profiles and those obtained by simulations run using Eclipse 100. Here, the relative permeability curves are estimated as functions of B-spline curves. The minimization of the difference in the saturation profile errors is based on modifying the relative permeability curves. This is done by altering the B-spline curves used to define these relative permeability curves. B-spline curves are updated by using the optimization method of simulated annealing. Figure 3-16 presents a flow chart that explains the method used. The calculations utilize a using a C++ project space developed by Schembre(2004). The

project space utilizes various sub routines to perform simulated annealing, estimation of relative permeability, and capillary pressure curves. The work space also interacts with Eclipse100 (GeoQuest). Relative permeability and capillary pressure curves developed by the workspace are written as '.inc' files that are utilized by Eclipse. We begin with an estimation of the relative permeability curves by choosing an initial set of B-spline curves. These are then used to develop relative permeability and saturation curves. Based on these curves we run a one dimensional Eclipse100 model.

The Eclipse simulation is constructed to model the experiment and is discussed in detail later. The saturation profiles calculated by Eclipse 100 are compared with experimental values. The error between these values is calculated by Equation 3-7.

$$E = \left[\frac{\sum_{0}^{N_{prof}} \sum_{1}^{N_{sat}} \left(x^{calc}\left(Sw_j, t_i\right) - x^{meas}\left(Sw_j, t_i\right)\right)^2}{\left(N_{sat} N_{prof}\right)^2} \right]^{\frac{1}{2}} \qquad 3\text{-}7$$

Here, E is the normalized error, N_{sat} is the number of saturation points, N_{prof} is the number of profiles, Sw_j is the j^{th} saturation and 'i' is the time. Also x_{calc} is the position estimated by ECLIPSE100 of the j^{th} saturation at time t_i. Similarly x^{meas} is the experimentally determined position of the j^{th} saturation at time time step t_i.

Based on the value of the error, the B-spline curves are updated using simulated annealing (Press, 2002). This process is repeated until the error given by equation 3-7 is below desirable values.

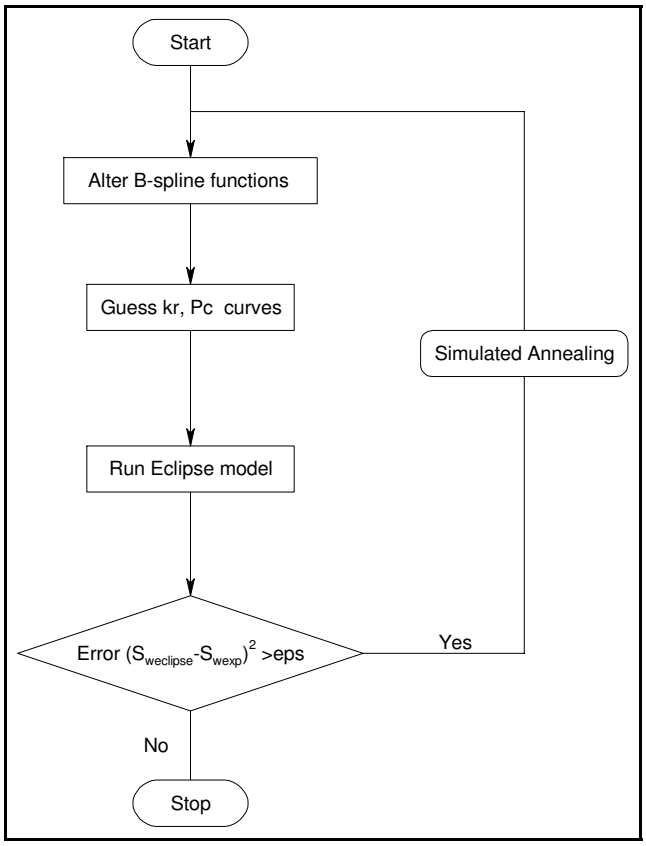

Figure 3-16: Flowchart explaining the method used in relative permeability estimation.

3.10. ECLIPSE Model

The flow simulation model consists of a single line of 101 blocks in the 'x' direction. There are no wells in the model. To model spontaneous imbibition the first block is assumed to be a fracture that feeds into the matrix of the remaining 100 blocks. The pore volume is multiplied by 100 times to get reasonable results The Eclipse model is run in lab units for the time of the experiment.

3.11. B-Spline Curves

While relative permeability curves for most permeable systems can be described by a power-law function, (i.e. Corey's model), these correlations do not provide satisfactory results for low permeability media such as coal. The method therefore models the relative permeability in its most general form possible. Relative permeability curves are modeled

using B-spline curves. B-spline curves are local 3 degree polynomial functions that define a continuous function over a given domain. Equation (3-8) defines a B-spline curve.

$$C(w) = \sum_{j=0}^{N} c_j B_{j,b}(w) \qquad \textbf{3-8}$$

Here ***w*** is a knot vector of length N+1; 'b' is the degree of the polynomial that in this case is 3. The parameters c_j are the control points and $B_{j,b}(w)$ are the basis spline functions based on the knot vector *wi* and *w*. A knot vector is a set of points where the value of the curve is predefined. Here we have a knot vector of 'N+1' points. As compared to a polynomial the B-spline curves provide additional N degrees of freedom. This is determined by the values we choose to give to the N+1 points. The polynomials between a set of two consecutive vector points are determined based on the following criteria:

- The second derivative of the spline curve is continuous at elements of the knot vector.
- The splines are equal to the knot vector values at the knot vector values.
- The spline curve generated is monotonic.

Using the above criteria, a basis for the spline curves is given by:

$$\begin{aligned} &B_{j,o}(w) = 1 \rightarrow if\left(w_i \le w \le w_{i+1}\right) \\ &else\left(B_{j,o}(w) = 0\right) \end{aligned} \qquad \textbf{3-9}$$

$$B_{j,b}(w) = \frac{w - w_j}{w_{j+b} - w_b} B_{j,b-1}(w) + \frac{w_{j+b+1} - w}{w_{j+b+1} - w_{j+1}} B_{j+1,b-1}(w) \qquad \textbf{3-10}$$

For our problem, we begin by defining the initial saturation control points. These are kept constant. Equations 3-9 and 3-10 help in defining the saturation vectors in terms of the basis functions for relative permeability and capillary pressure respectively.

$$S_w^i(w) = \sum_{j=1}^{N} S^i{}_j B_{j.b}^m(w) \qquad \textbf{3-11}$$

$$S_w^c(w) = \sum_{j=1}^{N} S_j^c B_{j.b}^m(w) \quad \textbf{3-12}$$

The relative permeability and the capillary pressure curves are then given by

$$k_{ri}(w) = \sum_{j=1}^{N} C_j^i B_{j.b}^m(w) \quad \textbf{3-13}$$

$$Pc(w) = \sum_{j=1}^{N} C_j^c B_{j.b}^m(w) \quad \textbf{3-14}$$

The coefficients in these curves are then varied with each iteration until the flow profiles from the simulation match experimental results within the prescribed tolerance.

3.12. Modeling of Non-Equilibrium Effects

The assumption of instantaneous equilibrium in low permeability porous media during spontaneous imbibition experiments is found to be inappropriate (Leguen & Kovscek 2006). We therefore used Schembre's method to model the non-equilibrium effects. The method involves utilizing Barenblatt's(2003) model to interpret the flow. The model suggests that the redistribution of the different phases in the pore space during imbibition is not instantaneous but takes some time 'τ'. When this redistribution time becomes important, the relative permeability and capillary pressure curves become process-dependent quantities. We then need to worry about the apparent saturation that reflects the actuality of the system. Using Bareblatt's(2003) we model the apparent saturation as :

$$\eta = S_w + \tau \frac{\partial S_w}{\partial t} \quad \textbf{3-15}$$

Here S_w is the measured saturation, τ is the average redistribution time, and τ can be obtained by matching the dimensionless non-wetting phase production with the predictions of Silin and Patzek (2004). This is given by the following equation

$$R(t) = V_o \left(1 - e^{\frac{t}{\tau}}\right) \sqrt{\frac{t}{\tau}} \quad \textbf{3-16}$$

V_o is characteristic of the fluid and the core.

Chapter 4

4. Results and Discussion

The theme behind these studies has been to try understand wettability at different scales. While earlier we looked at a theoretical development for understanding microscopic wettability, the experimental studies have been an effort at understanding wettabilty at core-scale. As suggested earlier this has been done by measuring macroscopic wettability in terms of contact angles using Handy's equation as well as relative permeability relationships. Solution pH was the main parameter examined to date. The pH set studied was 2,3, 7, 10 and 12.

4.1. Macroscopic Contact Angle

Figures 4-1 to 4.3 show spontaneous imbibition in the different cores prepared. The weight imbibed with square root time is plotted. Figure 4-1 illustrates weight gain profiles of cores made from the first process. Figure 4-2 and 4-3 display profiles for cores prepared by the second technique. The variation of linearity within Figure 4-1 suggests heterogeneity of the cores. It also teaches us that high pH such as 12 imbibes water at a much faster rate than the neutral and the acidic solution The linear portion of these profiles have been used for macroscopic profiles.

Figure 4-2 shows experiments done with a single core developed by the second process. Experiments at low pH (pH equal to 2), were repeated. The profile of the repeat experiment for pH 2 matches, substantially, the profile achieved in the first experiment. The system is also seen to be more water wet at pH equal to 2 then at pH equal to 10.

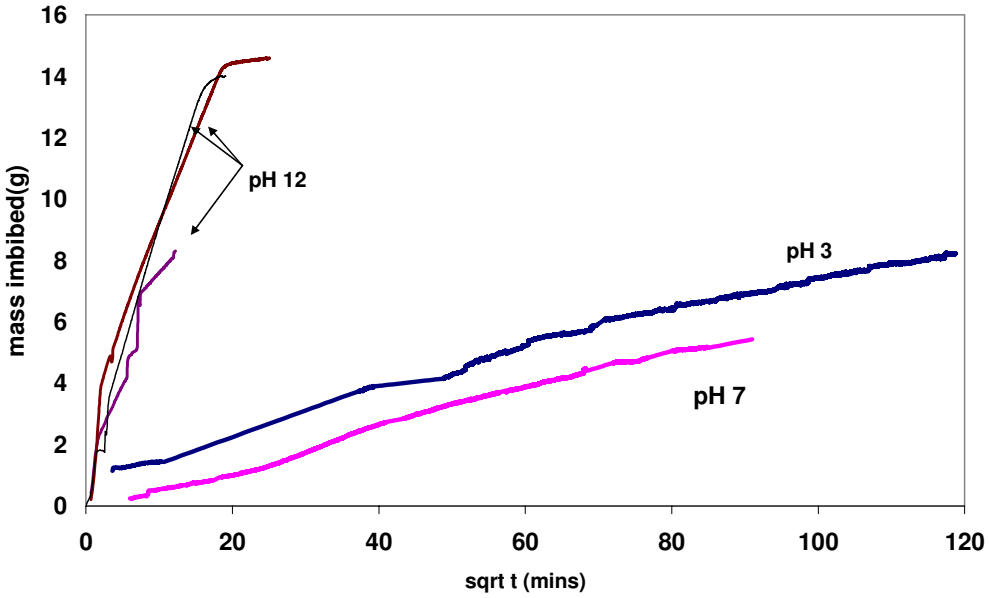

Figure 4-1: Mass imbibition at different pH with cores made from first method.

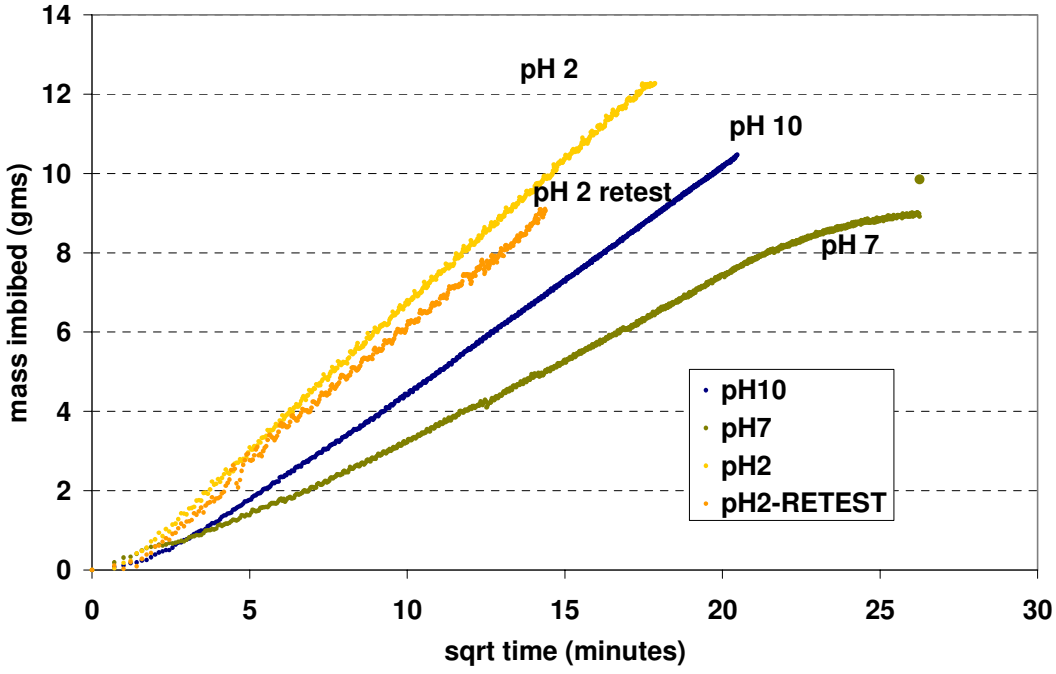

Figure 4-2: Mass imbibition at different pH with cores made from second method.

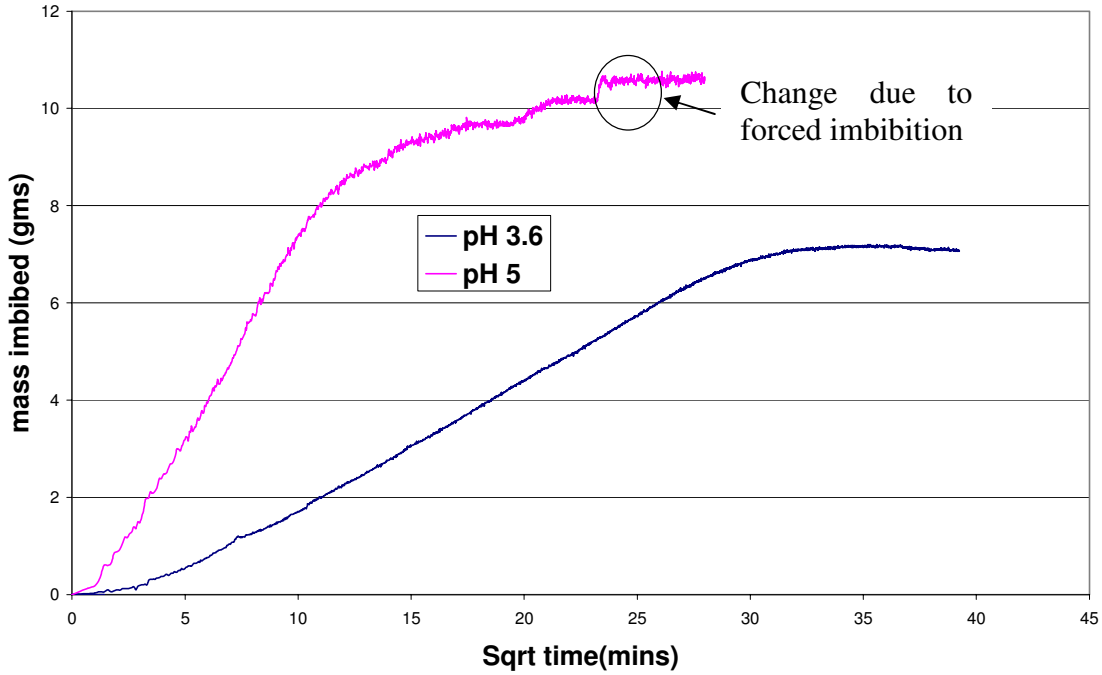

Figure 4-3: Mass imbibition at different pH with cores made from second method.

Figure 4-3 shows two more imbibition curves for low pH system. The results however suggest a different physics as compared to that suggested by DLVO theory. Here pH equal to 5 water solution seems to imbibe much faster than pH 3.6. This happens because the experiments have been carried out in two different cores. The permeability of the core that imbibed pH equal to 5 solution is about 5 times that of the other core. It therefore imbibes water at a much faster rate than the other core.

We now look at the results from all these experiments for macroscopic contact angle calculations. Using Handy's equation we get ratios of cosine of contact angles. To reduce these ratios to an absolute scale we need to make certain assumptions about wettability at high pH. As is seen from literature and theoretical calculations, at a very high pH coal systems are extremely water wet. We therefore assume that the contact angle at a high pH is 0 and the system is completely water wet. This allows us to estimate contact angles at varying pH. The results are shown below in Figure 4-4. Separate curves are constructed for the different cores used. For the core made by the press, we have used the contact

angle value at pH 2 as given in literature for lignite. (Refer Figure:2-3). This is also the contact angle value predicted by similar calculations for core 1.

We see that while the contact angles values do not match exactly those predicted by theoretical methods, the profiles are very similar. The stark variation in imbibition with pH has also been quantified in terms of contact angles. The imbibition studies also suggest a strong correlation between microscopic and core-scale wettability.

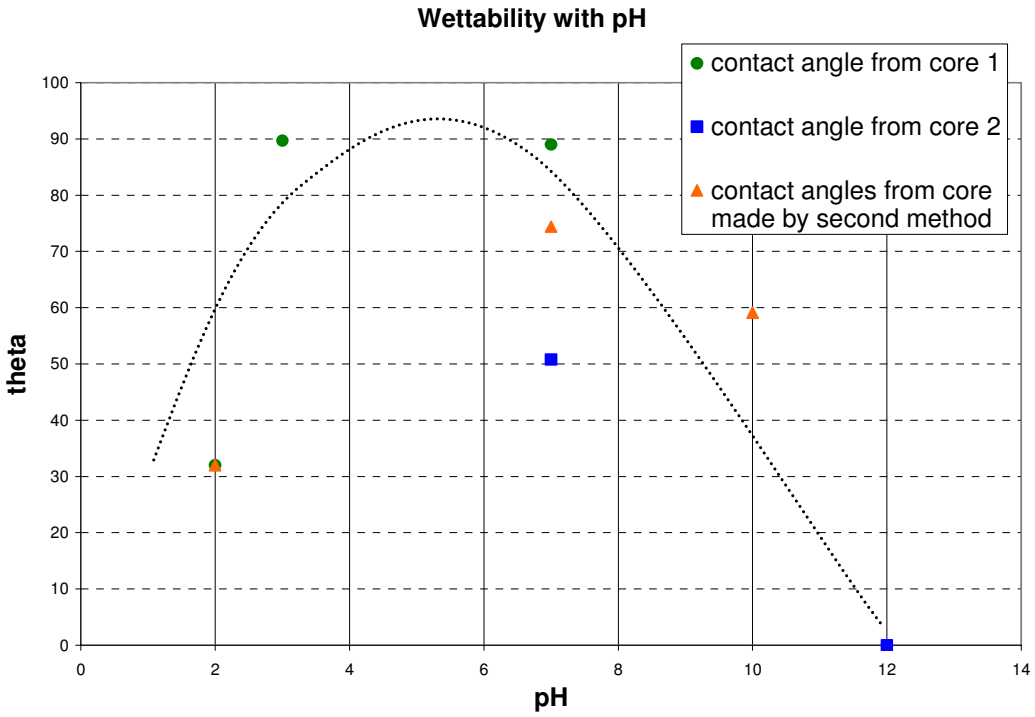

Figure 4-4: Macroscopic wettability with pH variation.

We have also calculated the Amott Indices for experiments at various pH. Table 4-1 lists these values. These values also suggest that the system is least water wet at a neutral solution. The wettability of the system increases rapidly with increasing acidity or alkalinity.

Table 4-1: Amott Indices at various pH

pH	2	3.6	5	7	10	12
Amott Index	0.965	0.974	0.958	0.837	0.957	0.988

4.2. Relative Permeability Estimations

We have also tried to understand wettability on a more universal scale. As suggested earlier, this was done by estimating relative permeability curves for water-air-coal systems. The relative permeability curves have currently been developed for pH 2, pH 7 and pH 10. Figure 4-5 describes the full one-dimensional saturation profile measured using CT scan images. The flow occurs in the image from right to left.

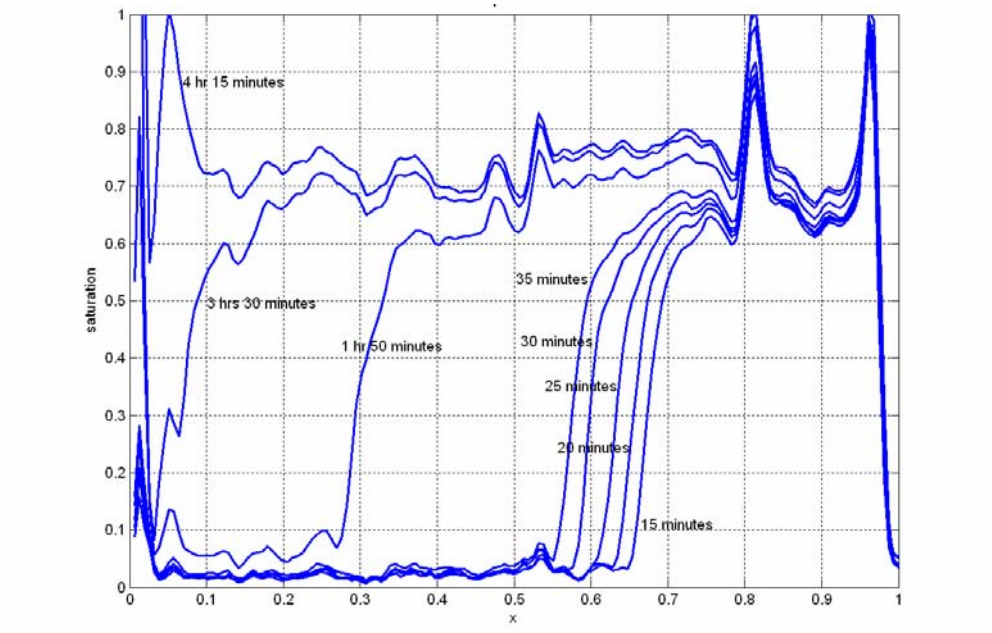

Figure 4-5: Saturation profiles with time for pH-2, flow is from right to left.

We see that at about 0.8 dimensionless lengths the saturation values once again reach 1. This is because of the presence of a fracture. The fracture developed with multiple uses of the same core. The drying of the core takes a long time. To reduce this period we therefore heat the core to about 35°C. This process has resulted in the presence of a fracture. To model the relative permeability curves, we therefore consider the saturation profiles from dimensionless lengths 0.0 to 0.8.

Figure 4-6 describes the saturation profiles achieved by an Eclipse simulation as compared to the experimental results. These results have been obtained by optimizing the relative permeability curves for the air-water system. In simulations, gas is non wetting.

Given the inaccuracies of the experiment and the differences in the experiment and the simulation model (square and rectangular flow) the saturation profiles for the relative permeability estimation are extremely similar to those obtained experimentally. A possible explanation for the inaccuracy in the saturation profile at longer times could be our simplifying assumption of a constant redistribution time. Redistribution time might vary with saturations and therefore at longer times, when the saturations are usually higher the redistribution would be much different and the shift achieved would be closer to the actual values. We have, however, tried and best fit a τ value for all times. For pH equal to 2 it was found to be 27 seconds. Figure 4-7 describes the optimized relative permeability curves obtained.

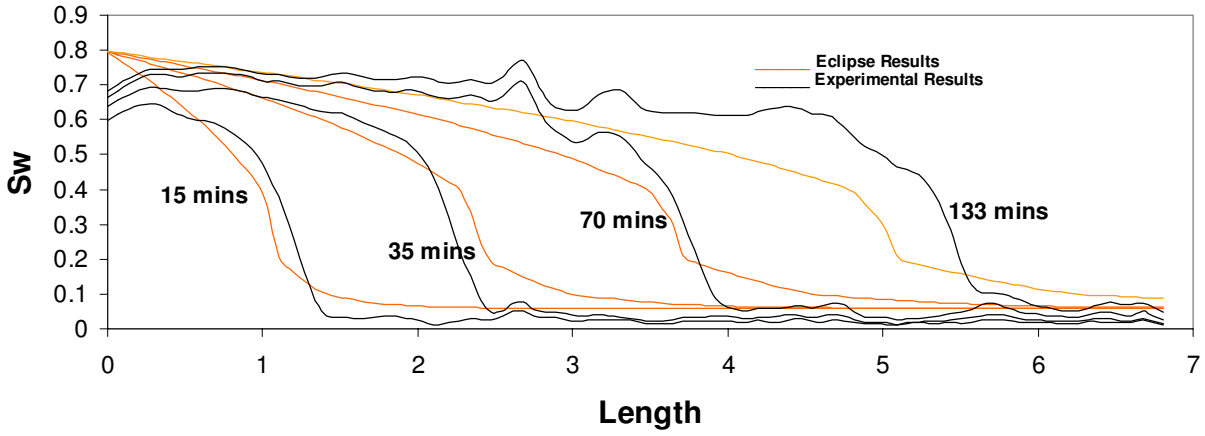

Figure 4-6: Simulation and experimental saturation profiles with time for pH-2.

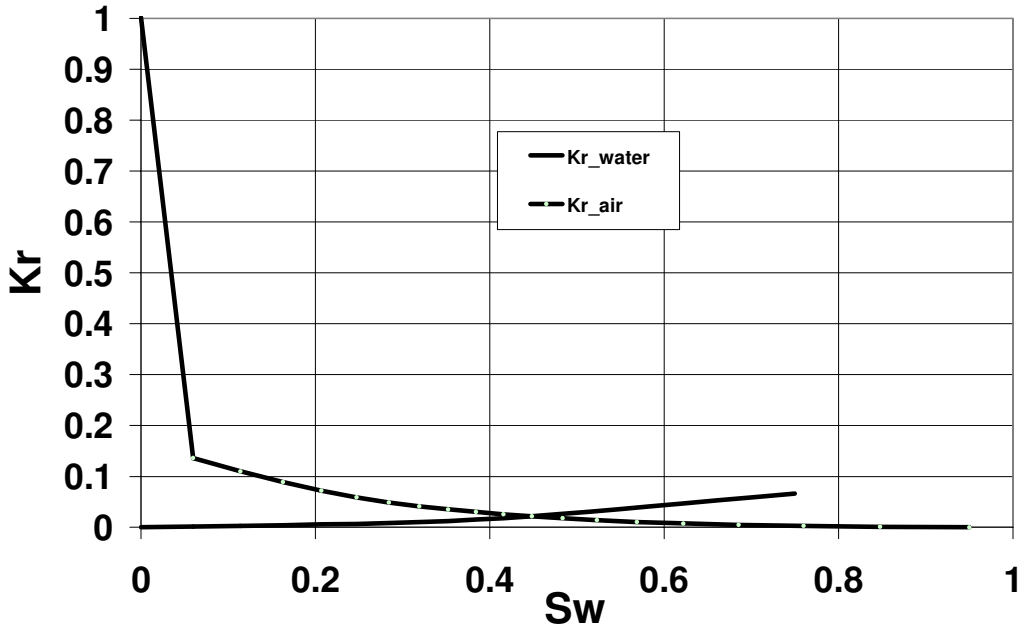

Figure 4-7: Relative permeability curves, pH equals 2, air/water/coal system.

The crossover point of the relative permeability curves as suggested by Figure 4-7 is less than 0.5. This suggests that the system is not extremely water wet. Another observation is that the endpoint values are very small. This is consistent with the fact that the system has low permeability. The relative permeability curves suggest an end point of 0.75 for gas. This is, however, untrue. This is because of the presence of the fracture. As water imbibing continuously feeds the fracture, the saturation in the fracture continues to change. We have modeled this as a constant saturation of 0.75. This value however increases up to 0.95. This suggests that the relative permeability curves estimated above should therefore have an end point at about 0.95. These calculations however do give an important insight about the shape of the relative permeability curves and also the wettability of the system.

Similar calculations were also done for pH equal to 10. Figure 4-8 displays the saturation profiles obtained experimentally and through simulations. The redistribution time for pH equal to 10 systems was found to be small. The calculations represented here assume that τ is zero. We see that the saturations up to 0.95 are mobile. The relative permeability

curves in Figure 4-9 substantiate this. Also the intersection point is shifted to the right suggesting that on the core-scale the system with pH equal to 10 is more water wet.

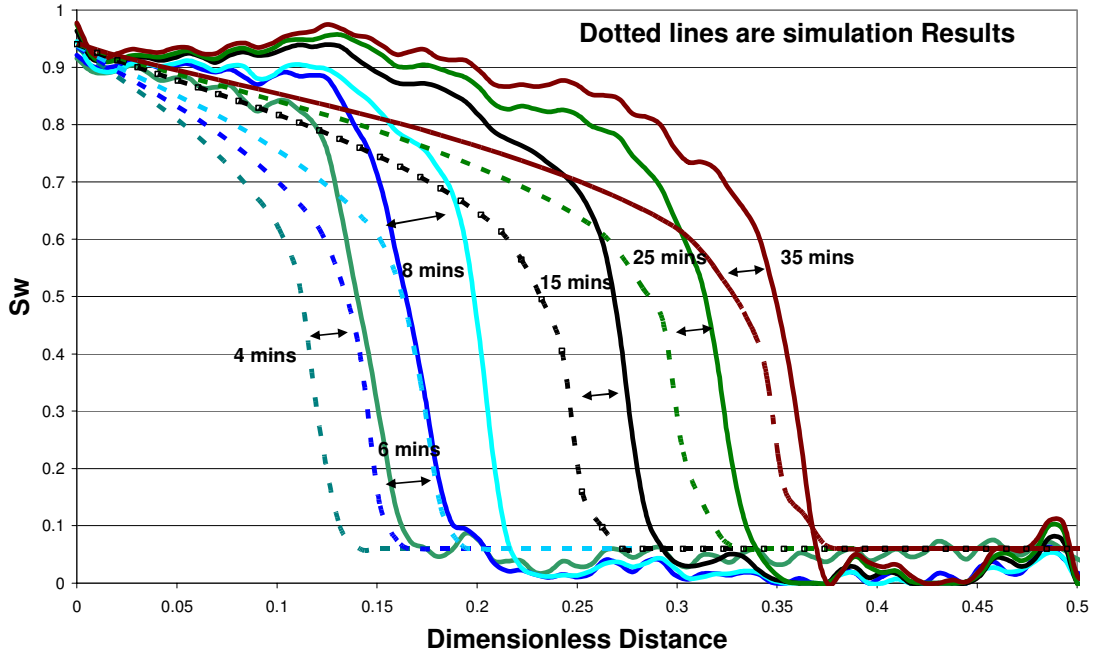

Figure 4-8: Simulation and experimental Saturation profiles for pH 10.

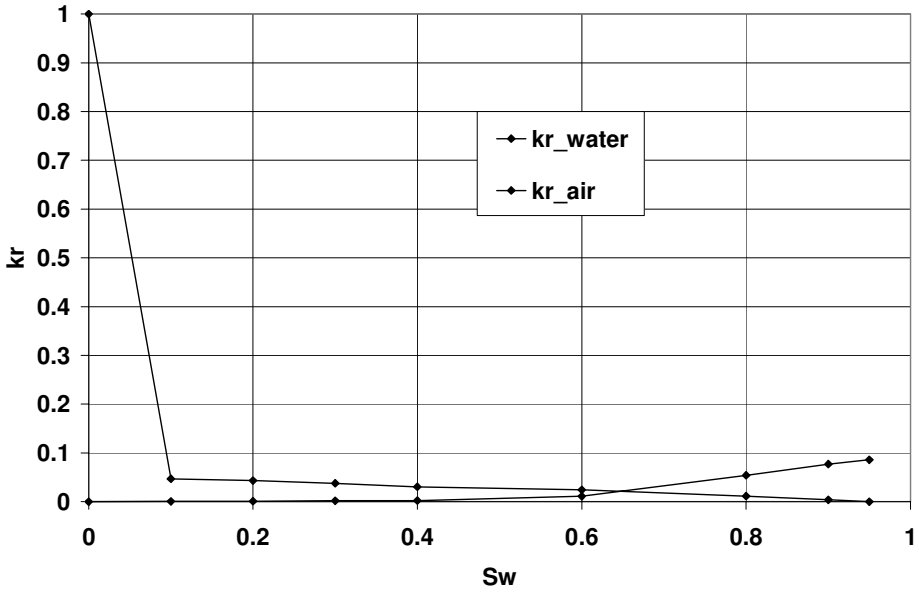

Figure 4-9: Relative permeability curves, pH equals 2, air/water/coal system.

Both the DLVO calculations and the water imbibition results suggest that at pH 7 the system is less water wet than at high pH. This is also seen in the relative permeability curves generated for pH 7 system. Figure 4-10 shows both the experimental and ECLIPSE generated flow profiles. The experimental profiles suggest a remarkable difference between spontaneous imbibition in a pH 7 system as compared to systems (high and low pH). Also the redistribution time 'τ' is much larger for this system with a value of 150 seconds. The match at longer times is found to be inaccurate. The relative permeability curves shown in Figure 4-11 however do agree with the discussion on DLVO theory as well as imbibition results, that systems with pH equal to 7 are less water wet than high or low pH systems.

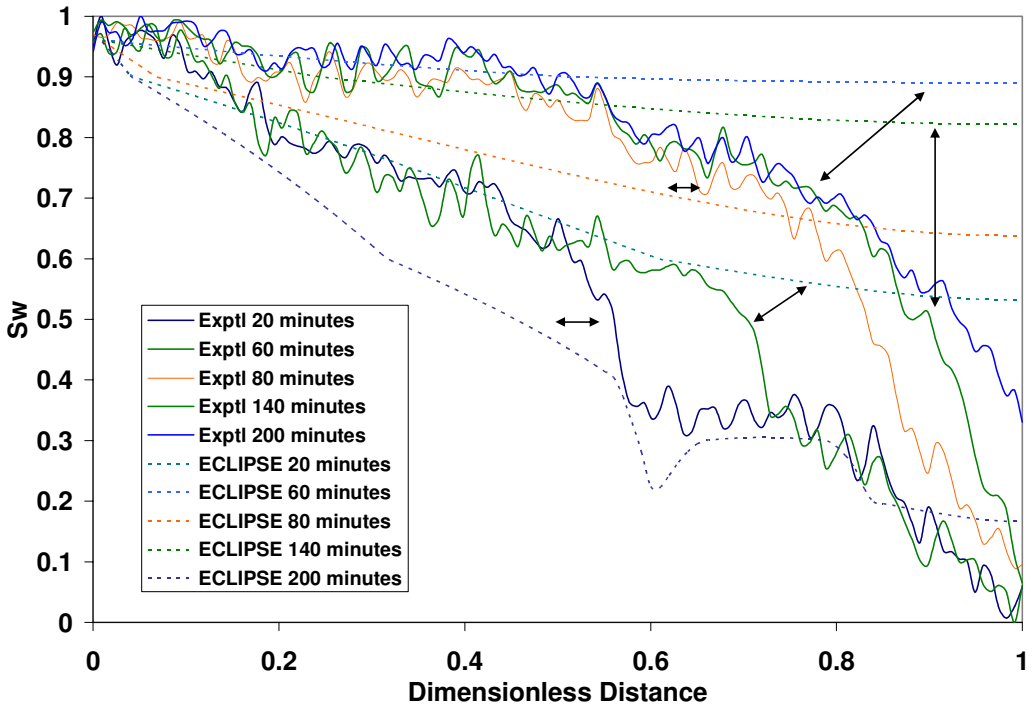

Figure 4-10: Experimental and Simulation Saturation Profiles for pH equal to 7.

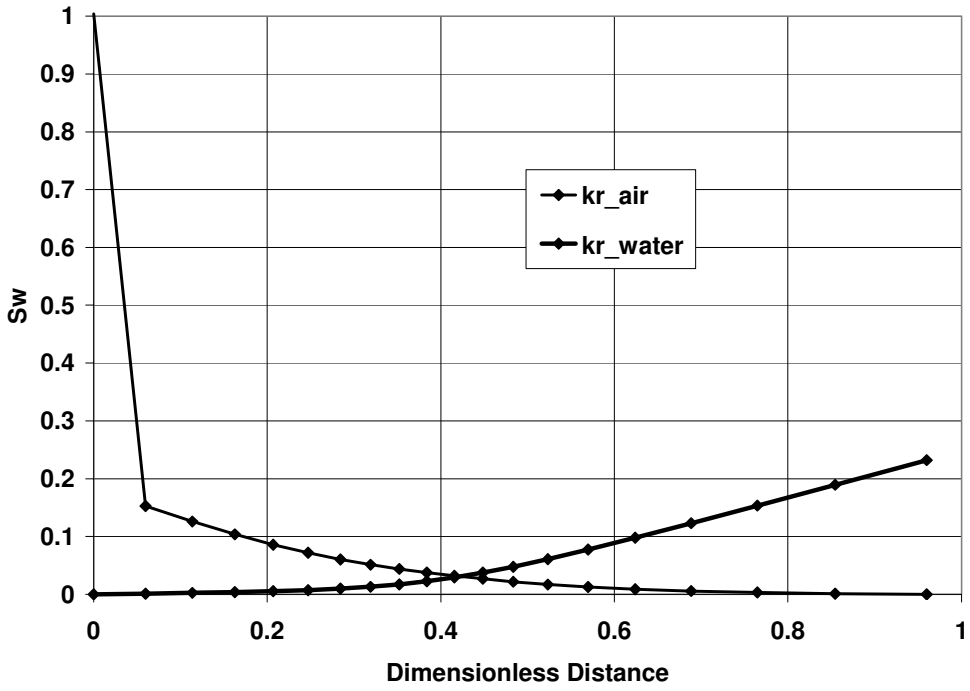

Figure 4-11: Relative permeability curves, pH equals 7, air/water/coal system.

4.3. Conclusions

We have studied wettability at various scales, ranging from the microscopic to core scale to reservoir scales. While contact angle measurements define wettability at microscopic and core scales, spontaneous imbibition tests and relative permeability curves are used to define wettability at reservoir scales.

Theoretical wettability calculations confirm literature trends that the contact angle does vary with the pH of the system. At extremely high acidity or alkanity coal-water systems seem to be strongly water wet. This would suggest that injection of CO_2 in coal beds might alter the wettability of the system by making it more acidic. The trends suggested show that the contact angle goes through a maximum at around pH 4. This value is for a specific coal water system. Theory suggests that the value of the location of the maximum varies depending on the coal system being studied. Our calculations also suggest that a

better grasp of the variation of the Hamaker constant with pH is important in understanding wettability variations with pH.

Our pore scale studies also show that the thin layers formed on the coal surfaces are constant potential rather than constant charge. Gregory (1980) suggests that in constant potential systems unequally charged surfaces always tend to be attractive. This is true even if the surfaces have charges of the same sign. Also the attraction decreases as the charge on the two surfaces approaches each other. This means that the thin film formed on a coal surface is weak when the charge on the two surfaces is unequal and it would be most stable when the charges are similar or equal.

The core-scale imbibition studies also provide us with another method to understand coal wetness. The strength of imbibition forces are gauged from the slope of the weight gain versus the square root of time. Our results suggest similarity in coal scale behavior with pore scale wettability. Imbibition is much stronger at higher pH. The rate of imbibition goes through a minimum at neutral pH and rises again at lower pH. Variation in imbibition rates with pH is of significant interest as coal systems consist of water of variable pH. These studies provide a stepping stone towards understanding water flow in coal systems.

Relative permeability curve estimates help in reservoir definition of the coal system. Curves have currently have been developed for pH equal to 2, 7, and pH equal to 10 systems. Results for the above pH solutions (2,7 and 10) show that the intersection point of the wetting and non-wetting phase relative permeability curves vary with pH. The intersection point has a highest value of water saturation (S_w=0.65) for pH 10 and least for pH equal to 7(S_w=0.43). These results also suggest that the coal-water-air system is most water wet at pH equal to 10 and least at pH equal to 7. However the very low values of both k_{rw} and k_{rnw} for large range of saturations suggest a mixed-wet nature of Powder River Basin coal.

While the results are encouraging as these are the first steps towards developing relative permeability curves for coal-methane and carbon-dioxide systems, further experiments with alternative pH systems with CO_2 in the pore space are required to develop a full understanding of wettability and multi-phase flow for these systems. Further, it would be interesting to see the behavior of an actual coal core as compared to a coal powder composite.

Nomenclature

A	Hamaker constant
A_s	Structural Force Constant
b	Degree of B-spline
$B_{j,b}(w)$	B-spline basis of degree b
c_j	Control point
C_i^j	ith control point for j function.
C_m	Interfacial curvature
CT_{var}	Computed Tomography number of medium 'var'
E	Objective function
e	Electronic charge
F_A	van der Waals attractive forces
F_d	Electrostatic force between the thin film surfaces
F_h	Structural (Hydration) force
h	Film thickness
h_o	Structural force decay length
$J(S_w)$	Leverett function at saturation 'S_w' of water.
k	Boltzmann constant
k_{ri}	Relative permeability of phase i
m	Number of interior points in B-splines
$n_{b...}$	Molar ion density
n_i	Refractive index of medium 'i'
N	Degree of freedom in B-spline definition.
N_{sat}	Number of saturation points
N_{prof}	Number of profiles
P_c	Capillary pressure
$R(t)$	Dimensionless air production
S_j^i	Control point for S_w

S_p	Saturation of phase ‘p’
t	Time
T	Temperature
V_o	characteristic volume depending on the system and the fluid
w_i	Component of the knot vector, W, in spline definition
x	Saturation position
$x^{calc}\left(Sw_j, t_i\right)$	Calculated saturation position of profile ‘j’ at the ith time step
$x^{meas}\left(Sw_j, t_i\right)$	Calculated saturation position of profile ‘j’ at the ith time step

Greek

ε	Dielectric permitivitty
φ_i	Reduced potential of surface ‘*i*’
κ	Debye length
λ	London wavelength
μ	Viscosity
$\pi(h)$	Disjoining pressure of film of thickness ‘*h*’
$\Pi(h)$	Disjoining pressure of film of thickness ‘*h*’
ρ_i	Density of fluid ‘*i*’
σ	Surface tension
τ	Redistribution time
ξ	Dimensionless distance
ζ_i	Surface potential

References

Akin, S., J. M. Schembre, S. K. Bhat, and A. R. Kovscek, "Spontaneous Imbibition Characteristics of Diatomite," *Journal of Petroleum Science and Engineering*, 25, 149-165, 2000.

Arnold, B. J. and Aplan, F. F., "The Hydrophobicity of Coal Macerals," Fuel, 68, 651-658, 1989.

Buckley J. S., Takamura K., and Morrow, N. R. "Influence of Electrical Surface Charges on the Wetting Properties of Crude Oils" SPE Reservoir Engineering 4, 332-340, 1989.

Churaev N. V., Derjaguin B. V., "Inclusion of Structural Forces in the Theory of Stability of Colloids and Films." Journal of Colloid & Interface Science, 103, 542-553, 1985.

Derjaguin, B. V. "Tiyra Kapillyarnoy Kondensatsii and Drugix Kapillapnvix Yavlenii Uchetom Rasklinivayuschchevo Daystiviya Polimolekulyarnox Shidix Plenok, Zh, Fiz Khim., 14, 137-147, 1940.

Gosiewska, A., Crelich, J, Laskowski, J. S., and Pawlik, M., "Mineral Matter on Coal Surface and Its Effect on Coal Wettability, J. Col. Interfac. Sci, 247, 107-116, 2002.

Gregory J. "Approximate Expressions for Retarded Van Der Walls Interactions" Journal of Colloid & Interface Science, 83, 138-145 1981.

Gutierrez-Rodriguez, J. A., Purcell, R. J. Jr., and Aplan, F. F., "Estimating the Hydrophobicity of Coal," Colloids and Surfaces, 12, 1-25, 1984.

Handy L.L., “Determination of effective capillary pressure for porous media from imbibition data.” Pet. Trans AIME 219 75-80, 1960.

Hirasaki, G. J., “Thermodynamics of Thin Films and Three-Phase Contact Regions,” in Interfacial Phenomena in Oil Recovery, Morrow, N. R. (ed), Marcel Dekker Inc,, New York, 23-76, 2000.

Israelachvili J. “Intermolecular & Surface Forces” Academic Press 2nd Edition 1991.

Kelebek S., Salman, T., Smith, G. W. “Interfacial Phenomena in Coal Floatation Systems.” Coal Symposium -1982. Proceedings 64th CIC., 145-152, 1982.

Karraker K.A., Radke C. J., “Disjoining Pressures, zeta potentials and surface tensions of aqueous non-ionic surfactant/electrolyte solutions: theory and comparison to experiment” Advances in Colloid and Interface Science, Vol. 96 2002.

Keeling CD, Whorf T.P., Wahlen M, Vanderplicht J.; “Interannual extremes in the rate of atmospheric carbon dioxide since 1980.” Nature 1995; 375(6533):666-70

Le Guen ,S. S, Kovscek A. R. ; “Non equilibrium Effects During Spontaneous Imbibition”. Transport in Porous Media, Vol 63, pg 127-146, 2006.

Li, C. and Somasundaran, P. “Reversal of Bubble Charge in Multivalent Inorganic Salt Solutions. Effect of Magnesium, J. Colloid Interface Science 146, 215-218, 1991.

Reeves S., “Assessment of CO2 Sequestration and ECBM Potential of U.S. Coabeds”, U.S. DOE, 2003.

Reeves S., “A Technical and Economic Sensitivity Study of Enhanced Coalbed Methane Recovery and Carbon Sequestration in Coal”, U.S. DOE, 2004.

Schembre, Josephina M., Temperature, surface forces, wettability and their relationship to relative permeability of porous media, PhD theses, STANFORD UNIVERSITY,2004

US Coal Reserves: A Review and Update; Energy Information Agency, August, DOE/EIA-0529(95) pp(1-17):1996

Valverde M. A. R. et al., "Stability of Highly Charged Particles: Bitumen-in-Water Dispersions" Colloids and Surfaces 222(2003) 233-251.

Weast, R.C., ed, CRC Handbook of Chemistry and Physics, E-56, Boca Raton, Fl, 1983.

Appendix A

A. FPI Scripts

This appendix list the scripts used to develop saturation and porosity profiles from CT numbers.

a) Script for Porosity

```
## Modified by Tanmay Chaturved December 2005
###This program calculates voxel by voxel porosity using the dery and fully saturated images
clear
print " POROSITY.IMP"
print " "
print " Disabling Auto Roi Processing"
viewer autoroi off
print " Enabling Auto Width/Level"
viewer autowinlev on
viewer caption "Porosity Calculations"
viewer notify
mask = 0
CTair = -1000.
CTwater = 0.
$dry_scan = "*.img"
$wet_scan = "*.img"
$destfile = "*.img"
getfile $wet_scan  " Select Wet Starting File"
getfile $dry_scan  " Select Dry Starting File"
getfile $destfile  " Select Output Starting File"
input images "Enter number of images to process"
ask masked "Do you want a circular mask?"
if masked = 1
  gosub setupmask
endif
#
# This the Main Processing Loop
#
clear
*MainProc
 if masked = 1
```

```
  gosub MaskedProc
 endif

 if masked = 0
  gosub UnMaskedProc
 endif
#
# Send Image to Viewer
#
 viewer clear
 viewer caption $destfile
 viewer display $destfile
 viewer notify
#
# Display statistics if masked.
#
 if masked = 1
  avg = accum / area
  print "Center Coords: (" cc_x "," cc_y ") Radius: " radius
  print "Pixels Calculated: " area "   Average Value: " avg
  print " "
  viewer pen 1 0 255 255 1
  viewer moveto 0 0
  viewer text "Pixels: " area "   Avg: " avg
  viewer draw
  viewer notify
 endif
#
# Increment filenames for next process
#
 nextfile $wet_scan
 nextfile $dry_scan
 nextfile $destfile
 if images > 1
  images = images - 1
  goto mainproc
 endif

#
# Processing completed
# Perform clean-up
#

 delete \fpimage\temp\circl.img
 viewer clear
```

```
 viewer tool arrow
 viewer caption "Porosity Calculations Completed."
 viewer paint
 viewer notify
 clear
 exit
#
#
# This Sub-Routine creates the circular mask
#
*SetUpMask
 gosub UnMaskedProc
 clear
 print " Enabling Line Tool..."
 print " "
 print "INSTRUCTIONS:"
 print " 1) Wait for an image to be displayed."
 print " 2) The Line Tool will be active."
 print " 3) Draw a line across the diameter of the "
 print "    of the circular mask"
 print " "
 viewer clear
 viewer tool arrow
 viewer tool line
 viewer display $destfile
 viewer notify
*RetryMask
 viewer clear
 viewer moveto 0 0
 viewer text " Draw a line across the diameter."
 viewer draw
 viewer notify
 print " Waiting for diameter coordinate pairs....."
  mousedown = 0
  mouseup = 0
*WaitForMouse
  if mousedown = 1
    mousedown = 0
    sx = mousex
    sy = mousey
  endif
  if mouseup = 1
    mouseup = 0
    ex = mousex
    ey = mousey
```

```
    goto calcmask
  endif
GOTO WaitForMouse

*CalcMask
  ulx = sx
  uly = sy
  lrx = ex
  lry = ey
  if sx > ex
    ulx = ex
    lrx = sx
  endif
  if sy > ey
    uly = ey
    lry = sy
  endif
  v = lry - uly
  h = lrx - ulx
  radius = sqrt((v * v) + (h * h)) / 2
  rad = radius * radius
  cc_x = ulx + (h / 2)
  cc_y = uly + (v / 2)

  print " Center Coords: (" cc_x "," cc_y ") Radius: " radius
  print " "

  infile_a $destfile
  outfile \fpimage\temp\circl.img
  process begin
    out = -1000000
    rim = ((xpos - cc_x) * (xpos - cc_x)) + ((ypos - cc_y) * (ypos - cc_y))
    if rad > rim
      out = ina
    endif
  process end

  viewer display \fpimage\temp\circl.img
  viewer notify
  ask again " Do you want to specify another mask?"
  if again = 1
    goto retrymask
  endif

RETURN
```

```
#
# This Sub-Routine is for a masked process
#

*Maskedproc

  infile_b $dry_scan
  infile_c $wet_scan
  infile_d \fpimage\temp\circl.img

  image_type = 1
  outfile $destfile
  ind = 0
  area = 0
  accum = 0
  process begin
    out = -10000
    if ind > -10000
      out = 0
      if inc ! inb
#       out = (inc - inb)/(CTwater - CTair)
        out = -1
      endif
      area = area + 1
      accum = accum + out
    endif
  process end
RETURN

#
# This Sub Routine is for a regular process
#
*UnMaskedProc
  infile_b $dry_scan
  infile_c $wet_scan

  image_type = 1
  outfile $destfile
  process begin
    out = 0
    if inc ! inb
        out = (inc - inb)/(CTwater - CTair)
#       out = -2
      endif
```

```
  process end
RETURN
```

b) Script for Saturation Profiles

```
#
#                                                Script to calculate the saturation values of images
#                                                      at the same location for different time steps
# Both wet_scan and $dry_scan do not change (since the location is fixed)
#
# Note: This script does not include the creation of circular masks
#
#
# Written by Edgar R. Rangel-German (July 1999)
# Modified by Josephina Schembre (April 2001)
# Modified by Tanmay Chaturvedi (December 2005)

clear
print " 2PHSAT_EDGAR.IMP"
print " "
print " Disabling Auto Roi Processing"
viewer autoroi off
print " Enabling Auto Width/Level"
viewer autowinlev on
viewer caption "Two Phase Saturation Calculations"
viewer notify

CTwater=0.
CTair=-1000.


$main_scan = "*.img"
$sat_scan = "*.img"
#$porosity_scan= "*.img"
$destfile = "*.img"
getfile $dry_scan "Select dry image"
getfile $main_scan " Select Main Starting File "
getfile $sat_scan  " Select Fully water saturated Starting File"
getfile $porosity_scan "Select porosity starting file"
getfile $destfile  " Select Output Starting File"
input images "Enter number of images to process"


#
# This the Main Processing Loop
#
```

```
clear
*MainProc

   gosub UnMaskedProc

#
# Send Image to Viewer
#
 viewer clear
 viewer caption $destfile
 viewer display $destfile
 viewer notify


#
# Increment filenames (only main scans) for next process
#
#
# nextfile $sat_scan
# nextfile $porosity_scan
 nextfile $main_scan
 nextfile $destfile


 if images > 1
   images = images - 1
   goto mainproc
 endif


#
# Processing completed
# Perform clean-up
#

 viewer clear
 viewer tool arrow
 viewer caption "Two Phase Calculations Completed."
 viewer paint
 viewer notify
 clear
 exit
#
# This Sub Routine is for a regular process
#
```

```
*UnMaskedProc
  infile_a $main_scan
  infile_b $sat_scan
  infile_c $porosity_scan
  infile_d $dry_scan

  image_type = 1
  outfile $destfile
  process begin
   out= 0
  if inc ! 0
#       out=(ina - inb )
#                                                          out=((ina - inb )/ ((ind - inb)))+.06
#                                                       out=((ina-inb)/(inc*(CTair-CTwater)))
       out=0.06
       out=out+((ina-ind)/(inc*(CTwater-CTair)))


   endif
#
#    out = ((ina - inb) / (ina - inb))
#    out = (ina-inb)/(inc*(CTwater-CToil))
#     out= ((ina - inb )/ (inc - ina))
#   out=inc
  process end
RETURN
```

Appendix B

B. Matlab Codes for 1-Dimensional Saturation Profile Generation

```
clear all;
%%%%This program computes 1-dimensional Saturation profiles from CT data
.
% % % % % By Tanmay Chaturvedi
%%%%%Modified: June 6th 2006
% % % % We load the CT number matrices as text files.
load '0230-01.txt' ;
load '0230-10.txt' ;
load '0230-11.txt' ;
load '0230-12.txt' ;
load '0230-13.txt' ;
load '0230-14.txt' ;
load '0230-15.txt' ;
load '0230-16.txt' ;
load '0230-17.txt' ;
load '0230-18.txt' ;
load '0230-19.txt' ;
load '0230-20.txt' ;
load '0230-61.txt'

% % % % % The relevant portion of the complete CT Picture is obtained
from
% the CT image by choosing the write coloumns and rows from the image.
ph2_01  =X0230_01(183:226,203:352);
ph2_10  =X0230_10(225:268,203:352);
ph2_11  =X0230_11(225:268,203:352);
ph2_12  =X0230_12(225:268,203:352);
ph2_13  =X0230_13(225:268,203:352);
ph2_14  =X0230_14(225:268,203:352);
ph2_15  =X0230_15(225:268,203:352);
ph2_16  =X0230_16(225:268,203:352);
ph2_17  =X0230_17(225:268,203:352);
ph2_18  =X0230_18(225:268,203:352);
ph2_19  =X0230_19(225:268,203:352);
ph2_20  =X0230_20(225:268,203:352);
ph2_61  =X0230_61(225:268,203:352);
dry_img=ph2_01;%%%%%%%The first image acts as the raw image
por_img=(ph2_61-dry_img)/1000;%%%%%%Beer law based equations to compute
porosity
sat_img01=.06+(ph2_01-dry_img)./(por_img)/1000;
%%%%%%%%%saturation matrix evaluation
sat_img10=.06+(ph2_10-dry_img)./(por_img)/1000;
sat_img11=.06+(ph2_11-dry_img)./(por_img)/1000;
sat_img12=.06+(ph2_12-dry_img)./(por_img)/1000;
sat_img13=.06+(ph2_13-dry_img)./(por_img)/1000;
sat_img14=.06+(ph2_14-dry_img)./(por_img)/1000;
sat_img15=.06+(ph2_15-dry_img)./(por_img)/1000;
```

```
sat_img16=.06+(ph2_16-dry_img)./(por_img)/1000;
sat_img17=.06+(ph2_17-dry_img)./(por_img)/1000;
sat_img18=.06+(ph2_18-dry_img)./(por_img)/1000;
sat_img19=.06+(ph2_19-dry_img)./(por_img)/1000;
sat_img20=.06+(ph2_20-dry_img)./(por_img)/1000;
sat_img61=.06+(ph2_61-dry_img)./(por_img)/1000;
%%%converting matrix to vectors, adding up saturation along the
%perpendicular to  the flow direction
sat_img01= sat_calc(sat_img01);
sat_img10= sat_calc(sat_img10);
sat_img11= sat_calc(sat_img11);
sat_img12= sat_calc(sat_img12);
sat_img13= sat_calc(sat_img13);
sat_img14= sat_calc(sat_img14);
sat_img15= sat_calc(sat_img15);
sat_img16= sat_calc(sat_img16);
sat_img17= sat_calc(sat_img17);
sat_img18= sat_calc(sat_img18);
sat_img19= sat_calc(sat_img19);
sat_img20= sat_calc(sat_img20);
plot((1:150)/150,sat_img01);
hold on
plot((1:150)/150,sat_img01);
plot((1:150)/150,sat_img10);
plot((1:150)/150,sat_img11);
plot((1:150)/150,sat_img12);
plot((1:150)/150,sat_img13);
plot((1:150)/150,sat_img14);
plot((1:150)/150,sat_img15);
plot((1:150)/150,sat_img16);
plot((1:150)/150,sat_img17);
plot((1:150)/150,sat_img18);
plot((1:150)/150,sat_img19);
plot((1:150)/150,sat_img20);


function X = sat_calc(X)
%%%%%%%%%%%This function reads porosity and saturation vectors and
% % % % % % % % eliminates those that hav edivision by '0' or 'inf at
their
% voxel locations
A=isfinite(X);
for i =1:size(X,2)
    sat(i)=0;
    ctr(i)=0;
    for j = 1 : size(X,1)
        if (A(j,i)~=0)
            sat(i) = sat(i) + X(j,i);
            ctr(i)=ctr(i)+1
        end
    end
    if (ctr(i) ~= 0)
        sat(i)=sat(i)/ctr(i);
    else
        sat(i)=sat(i)/size(X,1);
    end
end
X=sat;
```

Appendix C

C.Sample ECLIPSE 100 File for Relative Permeability Usage

```
-- ************************************************************************
-- ECLIPSE FILE FOR IMBIBITION
-- Josephina Schembre   May 2001
-- Modifications
-- COUNTER-CURRENT IMBIBITION OUTCROP CORE 180 F
-- Modified by Tanmay Chaturvedi
-- January 2006
--Modifications
--Set up for Coal Packs to develop water-air relative permeability
-- ************************************************************************
RUNSPEC
NOECHO
TITLE
  INITIAL SW WITH FRACTURE NON-COMUNICATED IN X- AND WELL
DIMENS    -- dimension or block model
  1  1  101 /
OIL
WATER
GAS
LAB
```

```
EQLDIMS   -- equilibration table size
   1  100   10    1   20 /
TABDIMS   -- size of saturation tables
   2    1   50  12    3   12 /
START     -- simulation start
  1 JAN 2001 /
GRIDOPTS
YES 1 0 /
GRID
DX
  101*2.2155555  /
DY
   101*2.2155555  /
DZ
   1*1.
   100*0.086/
OLDTRAN
---
BOX
---   IX1-IX2  JY1-JY2   KZ1-KZ2
1  1      1  1     1   1     /
PERMX
   1*1000 /
PERMY
   1*1000 /
PERMZ
```

```
   1*1000  /
PORO
   1*10. /
---
BOX
---   IX1-IX2   JY1-JY2   KZ1-KZ2
     1    1     1   1     2  101    /
PERMX
   100*15 /
PERMY
   100*15 /
PERMZ
   100*15  /
PORO
    100*0.19 /
BOX
-------- IX1-IX2 JY1-JY2 KZ1-KZ2
1 1  1  1  1   1 /
MULTPV
1*1E2 /
---   TOP Specification
BOX
---   IX1-IX2   JY1-JY2  KZ1-KZ1
1  1     1   1    1  1 /
TOPS
    1*1. /
```

```
RPTGRID
 0 0 0 0 0 1 0 0 0 1 0 0 1  /
PROPS
--------------------------------
INCLUDE
'SIMPLE_WOG.INC'/
INCLUDE
'SWOF.INC' /
RPTPROPS
     2*1 0  2*1 0 2*1    /
REGIONS
INCLUDE
'REGIONS.INC' /
RPTREGS
     0  1  0  1  1  1 /
SOLUTION
--------------------------------
DATUM
1.1075 /
SWAT
     1*1.0
     100*0.06 /

SGAS
101*0.0 /
PRESSURE
--
       101*1.00 /
RPTSOL
     1 0 1 1 0 0 2  7*0  0  0  0  0 /
```

```
SUMMARY
----------------------------------------
RUNSUM
EXCEL
NARROW
RPTONLY

-- This is the file that dictates which parameter we want to print

INCLUDE
'BLOCKS100.INC' /

-- SUMMARY REPORT
--RPTSMRY
--1  /

--Turn on run summary at end of PRT file.
RUNSUM
SCHEDULE
----------------------------------------

TUNING
  .000277  0.6  0.00277 / -- middle one 0.05
  /
   /
--DEBUG
--0 1 11* 1 /
NOECHO
TSTEP
0.011111111
0.033333333
0.05
0.066666667
0.083333333
0.1
0.116666667
0.133333333
0.166666667
0.25
0.333333333
/
END
```

Appendix D

D. Matlab Code for DLVO Calculations

```
% This program computes contact angle values based on DLVO theory
% Inputs include zeta potential/ reduced potential , salinity,
% Variable parameters Include Hamaker Constant, Structural Constants
London's wavelength
%Contact Angles are computed for constant charge , constant potential
and
%the super position case
%Calculations are based on varying value of limiting thickness
(estimated
%thin film thickness)
%By tanmay chaturvedi
%last modified June 1st 2006
clear
clc
A=10*10^-20;               %Defining the Hamaker constants
lam=10^-7;
K=1.38*10^-23;
T=300;
N=6.023*10^23;
Elecperm=7.08*10^-10;    %%%%%%water dielectric permitivity
e=1.6*10^-19;
Asone=1.5*10^10;        %%%%%%structural constants
Astwo=1.5*10^11;  %%altered to power of 11
Asthree=1.5*10^12;
hs=.05;             %structural force parameter
L_bnd= 0.11;
U_bnd=100;
X=L_bnd:0.01:U_bnd;
%%disp(X);
ctr=(U_bnd-L_bnd)*100+1;
Fvw=zeros(ctr,1);
Fdch=zeros(ctr,1);
Fdpot=zeros(ctr,1);
Fdpot_lsa=zeros(ctr,1);
Fh=zeros(ctr,1);
for i=1:ctr                          %%%%%van der Walls and structural
force calculation
    Fvw(i,1)=-1*A*(10^-9*15.96/lam*X(1,i)+2)/(12*10^-
27*3.14*(X(1,i)*X(1,i)*X(1,i))*(1+5.32*10^-9*X(1,i)/lam)^2);
    Fhone(i,1)=Asone*exp(-X(1,i)/hs);
    Fhtwo(i,1)=Astwo*exp(-X(1,i)/hs);
    Fhthree(i,1)=Asthree*exp(-X(1,i)/hs);
end;
mol_conc=.1;%input('Enter the molar concentration of the solution');
ion_numb=2; %input('Enter the number of ions formed');
zeta=[-0.023    0.02423
-0.033  0.01467
-0.034  -0.01563
-0.039  -0.04813
```

```
-0.05   -0.08357
-0.075  -0.09033];
ch=length(zeta);
for i=1:ch
     phi1=e*zeta(i,1)/K/T;
     phi2=e*zeta(i,2)/K/T;
     Nb=N*1000*ion_numb*mol_conc;
     Inv_length=(2*e^2*Nb/Elecperm/K/T)^0.5;
     cond=0;%cond=input('Enter 1 for constant charge and 0 for constant
potential state');
        for i=1:ctr
            Fdpot(i,1)=Nb*K*T*(2*phi1*phi2*cosh(Inv_length*X(1,i)*10^-
9)-phi1^2-phi2^2)/(sinh(Inv_length*X(1,i)*10^-9))^2;
            Fdch(i,1)=Nb*K*T*(2*phi1*phi2*cosh(Inv_length*X(1,i)*10^-
9)+phi1^2+phi2^2)/(sinh(Inv_length*X(1,i)*10^-9))^2;
            Fdpot_lsa(i,1)=64*Nb*K*T*tanh(phi1/4)*tanh(phi2/4)*exp(-
1*Inv_length*X(1,i)*10^-9);
        end
        if cond==0
            DisjPone=Fvw+Fdpot+Fhone;
            DisjPtwo=Fvw+Fdpot+Fhtwo;
            DisjPthree=Fvw+Fdpot+Fhthree;
            DisjPone_lsa=Fvw+Fdpot_lsa+Fhone;
        else
            DisjPone=Fvw+Fdch+Fh;
            DisjPtwo=Fvw+Fdch+Fhtwo;
            DisjPthree=Fvw+Fdch+Fhthree;
        end
        plot(X',DisjPone,'r');
        hold on
        disp('the angle values for As=10^10');
        %thetaone=integral(DisjPone);
        thetaonebeta=integralbeta(DisjPone);
        disp('the angle values for As=10^6');
        %thetatwo=integral(DisjPtwo);
        thetatwobeta=integralbeta(DisjPtwo);
        disp('the angle values for As=10^12');
        %thet3=integral(DisjPthree);
        thetathreebeta=integralbeta(DisjPthree);
        disp('the angle values for As=10^10 for lsa ');
        thetaone_lsa=integral(DisjPone_lsa);
end


function theta=integralbeta(DisjPin)
%%%Evaluates contact angle based on Derjaguin equation
%%support function for reviseddlvo.m
X=.11:0.01:100;                 %%%%thickness
n=length(X);
q=max(DisjPin(59:n));
D3=DisjPin(19:n);   %%%%%first set of calculations strt assuming 3nm as
film thickness
X3=X(19:n);
D4=DisjPin(29:n);   %%%%assuming limit thickness as 4 nm
X4=X(29:n);
%disp(X4);
%disp(D4);
D5=DisjPin(39:n); %%%%%%assuming 5 nm and so on
X5=X(39:n);
D6=DisjPin(49:n);
```

```
X6=X(49:n);
D9=DisjPin(79:n);
X9=X(79:n);
D10=DisjPin(89:n);
X10=X(89:n);
%%for d3
Int3=10^-9*cumtrapz(X3',D3,1);     %%%%integral calculation
%if (q<=0 & q>-100)
 %   value3=1+20*(Int3(n-19);
 %else
    value3=1+20*(Int3(n-19)+10^-9*X3(1,1)*D3(1,1));
    %end;

if value3>1
    theta(1,1)=90;
elseif value3 <-1
    theta(1,1)=180;
else
theta(1,1)=acos(value3)/3.14*180;
end;

%%for d4

Int4=10^-9*cumtrapz(X4',D4,1);
value4=1+20*(Int4(n-29)+10^-9*X4(1,1)*D4(1,1));
if value4>1
    theta(2,1)=0;
elseif value4 <-1
    theta(2,1)=180;
else
theta(2,1)=acos(value4)/3.14*180;
end;
%%for d5
Int5=10^-9*cumtrapz(X5',D5,1);
value5=1+20*(Int5(n-39)+10^-9*X5(1,1)*D5(1,1));
if value5>1
    theta(3,1)=0;
elseif value5 <-1
    theta(3,1)=180;
else
theta(3,1)=acos(value5)/3.14*180;
end;
%%disp6
Int6=10^-9*cumtrapz(X6',D6,1);
value6=1+20*(Int6(n-49)+10^-9*X6(1,1)*D6(1,1));
if value6>1
    theta6(4,1)=0;
elseif value6 <-1
    theta(4,1)=180;
else
theta(4,1)=acos(value6)/3.14*180;
end;
%%disp 9
Int9=10^-9*cumtrapz(X9',D9,1);
value9=1+20*(Int9(n-79)+10^-9*X9(1,1)*D9(1,1));
if value9>1
    theta(5,1)=0;
elseif value9 <-1
    theta(5,1)=180;
else
```

```
theta(5,1)=acos(value9)/3.14*180;
end;
%disp(theta);
Int10=10^-9*cumtrapz(X10',D10,1);
value10=1+20*(Int10(n-89)+10^-9*X10(1,1)*D10(1,1));
if value10>1
    theta(6,1)=0;
elseif value9 <-1
    theta(6,1)=180;
else
theta(6,1)=acos(value10)/3.14*180;
end;
disp(theta);
```